INL/RPT-23-74593
Revision 0

Light Water Reactor Sustainability Program

Novel Approaches and Technologies for Aging Management

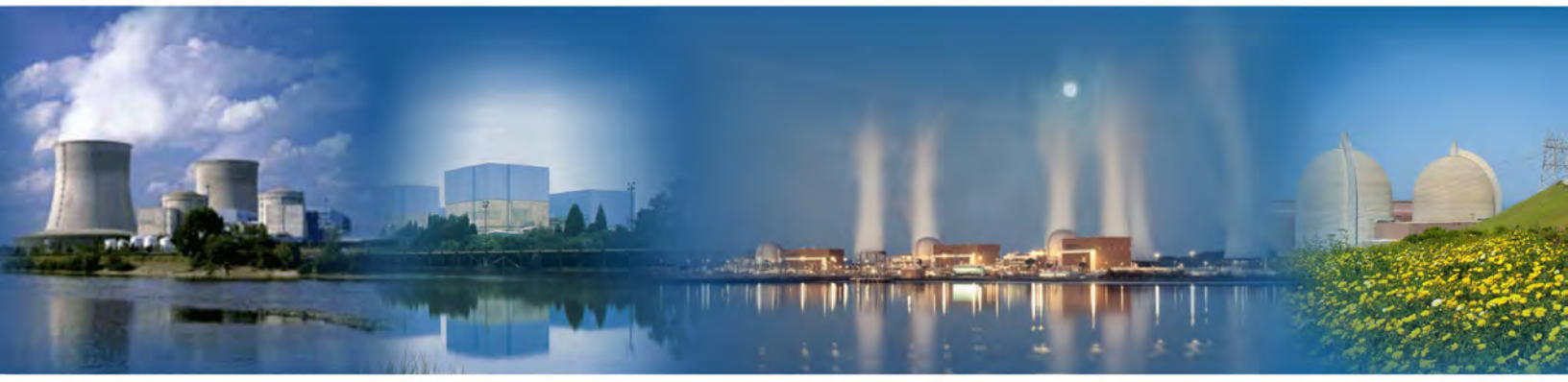

September 2023

U.S. Department of Energy

Office of Nuclear Energy

INL/RPT-23-74593
Revision 0

Novel Approaches and Technologies for Aging Management

Svetlana Lawrence, Vaibhav Yadav, Daniel Schwen, Daniel van Wasshenova, Jiheon Jun, James R Keiser, John E. Wade IV, Xiang Chen, Dongjin Du, Pranav Karve, and Sankaran Mahadevan

September 2023

Idaho National Laboratory
Idaho Falls, Idaho 83415

lwrs.inl.gov

Prepared for the
U.S. Department of Energy
Office of Nuclear Energy
Under DOE Idaho Operations Office
Contract DE-AC07-05ID14517

Page intentionally left blank

ABSTRACT

As part of the application process for license renewal and subsequent license renewal, nuclear utilities must perform an evaluation to confirm that the renewal scope appropriately considers aging effects on plant structures, systems, and components. This effort within the Light Water Reactor Sustainability program's Risk-informed System Analysis pathway is focused on risk-informed and performance-based approaches for aging management of buried piping, specifically managing selective leaching degradation phenomena. Selective leaching is a commonly occurring aging and degradation mechanism in buried pipes at nuclear power plants. To better understand the extent of selective leaching and its effect on the health of buried components, the licensees currently rely on visual inspections and destructive examinations which require extraction of multiple buried components, e.g., pipes. This research explores technological solutions that may replace or supplement existing inefficient, costly, and labor-intensive methods used in aging management.

ACKNOWLEDGEMENTS

The authors would like to acknowledge support of this project provided by Electrical Power Research Institute for providing valuable data, component samples, proprietary reports, and subject matter expertise. We especially appreciate time and expertise of Mr. Dylan Cimock, EPRI's Sr. Technical Leader.

Page intentionally left blank

CONTENTS

FIGURES

TABLES

ACRONYMS

2-D	two-dimensional
3-D	three-dimensional
AI	artificial intelligence
CSV	Comma Separated Values
DCI	ductile cast iron
EPRI	Electrical Power Research Institute
FE	Finite Element
FEM	Finite Element Method
FTCS	Forward in time centered in space
GCI	gray cast iron
INL	Idaho National Laboratory
MOOSE	Multiphysics Object-Oriented Simulation Environment
NDE	Nondestructive evaluation
NPP	Nuclear Power Plant
ORNL	Oak Ridge National Laboratory
PDE	Partial Differential Equations
PNG	Portable Network Graphics
SLR	Subsequent license renewal
XFEM	eXtended Finite Element Method

Page intentionally left blank

NOVEL APPROACHES AND TECHNOLOGIES FOR AGING MANAGEMENT

1. INTRODUCTION

The license renewal and subsequent license renewal (SLR) processes, defined in 10 CFR 54, provide a framework for U.S. nuclear power plants (NPPs) to extend their operating licenses. However, the current SLR process is very costly, time consuming, and resource-intensive. The research described in this report was conducted under the Light Water Reactor Sustainability program funded by the U.S. Department of Energy. This project evaluated novel approaches and technologies to reduce known burdens and costs associated with SLRs to help the operating nuclear fleet remain economically sustainable while maintaining the highest levels of safety.

The sections of this report are organized as following:

- Section 2 discusses modeling and simulation of structures with observed degradation using finite element modeling
- Section 3 provides an overview of laboratory experiments conducted with the goal to better understand selective leaching phenomena
- Section 4 presents an overview of available monitoring techniques and suggests options to use advanced monitoring techniques to supplement detection of degradation in buried components.

2. MOOSE-BASED MODELING: SELECTIVE LEACHING

Selective leaching, or selective corrosion, is the process by which one element from an alloy is removed. Graphite corrosion is the selective leaching process for gray cast iron (GCI) in which a brittle graphite shell remains after the dissolution of iron. The remaining shell leaves little visual evidence of change in structural dimensions or strength. Due to a considerable amount of GCI being used for water piping, this corrosion process is of concern for underground use. While inspection and monitoring has paths for dealing with this aging mechanism, computational modeling offers a method of prediction without the need of visual inspection.

MOOSE (Multiphysics Object-Oriented Simulation Environment), [1,2] a parallel computational framework that solves systems of coupled nonlinear partial differential equations (PDEs), was leveraged in modeling selective leaching. MOOSE, developed by Idaho National Laboratory (INL), is an open-source, parallel finite element (FE) framework primarily written in C++, which comes with several physics modules. The flexibility of the modules allows for the concurrent coupling of different physics.

The benefits of modeling within MOOSE come from the ease at which additional physics models can be applied. Using a unified input system and a mesh structure allows for future investigations to be added with minimal effort. The application of new physics can be done through modules within MOOSE or apps that are built upon the MOOSE framework. A select table of the modules and apps is shown in Table 1.

One such module, Tensor Mechanics, is a library of simulation tools that solve continuum mechanics problems. This module provides a simple approach for implementing simple to advanced mechanics models with the benefits of a plug-n-play design. This design enables users to incorporate the relevant physics for specific and varied conditions as needed. Additionally, this module can be used to simulate both linear and finite strain mechanics, including elasticity, creep, plasticity, and damage due to cracking.

MOOSE additionally can create meshes internally to run simulations. While external mesh generators can create complex geometries, using MOOSE avoids licensing issues and adds flexibility for working on the fly. Several classes exist which help in the simplified construction and refinement of meshes. Additionally, a separate module, XFEM, [3] allows for modeling fractures, material interfaces, and other discontinuities.

2.1 Developing MOOSE Simulation

2.1.1 Preliminary Development

A workflow was developed to facilitate solid mechanics modeling of degraded pipes in MOOSE. Electrical Power Research Institute (EPRI) conducted a study of an extracted GCI pipe that had undergone graphite corrosion. From this study a two-dimensional (2-D) laser scan depth data of sandblasted corroded pipes needed to be applied to a three-dimensional (3-D) model of a pipe. This laser scan data prescribes a material removal from the surface of the cylindrical pipe while assuming cylindrical symmetry for the undeformed mesh.

To map the relative change in height from the laser scan data, a new MOOSE object was developed to modify cylindrical pipe meshes for applying surface geometry. While the actual data from EPRI were pending, work commenced using a synthetic data set. This synthetic data method utilizes a 2-D grayscale image applied via the MOOSE framework onto a 3-D mesh. The grayscale images were created by simply utilizing a “spray paint” Portable Network Graphics (PNG) image, as seen in Figure 1, which was blurred to account for smooth changes in elevation between pixels.

Making use of MOOSE framework classes and custom developed objects that translate images into functions, this grid was applied as displacement boundary condition on the cylindrical surface. Using the displacement boundary conditions, a diffusion problem was solved on the displacement variables on the mesh interior. Additionally, the surface-driven displacement was smoothed out to maintain a reasonable mesh quality. This resulted in the displaced mesh with the laser scan geometry baked into a new mesh file.

Table 1. Modules within and apps developed on the MOOSE framework.

Module	Apps
Chemical Reactions	Pika
Combined	HOGNOSE
Contact	MAMBA
Electromagnetics	Hyrax
Fluid Properties	Ferret
Fluid-Structure Interaction	GRIME
Functional Expansion Tools	Gardensnake
Geochemistry	Zapdos
Heat Conduction	Moltres
Level Set	DGOSPREY
Misc.	Dendragapus
Navier-Stokes	Slug
Optimization	Redback
Peridynamics	MARMOT
Phase Field	RATTLESNAKE
Porus Flow	BISON
Ray Tracing	RELAP7
Reactor	PRONGHORN
Reconstructed Discontinous Galerkin	MAMMOTH
Richards	YAK
Solid Properties	OSPREY
Stochastic Tools	BIGHORN
Tensor Mechanics	BlackBear
Thermal Hydraulics	Grizzly
XFEM	Griffin

On the new mesh, solving can be done for mechanical stresses and strains using the Tensor Mechanics module. with given pressure boundary conditions applied to the pipe interior, as shown in Figure 2 and Figure 3. This method can be exploited in the future to simulate additional damaged pipes by creating simulated PNG damage images to further expand the data set on which the strains and stress can be evaluated.

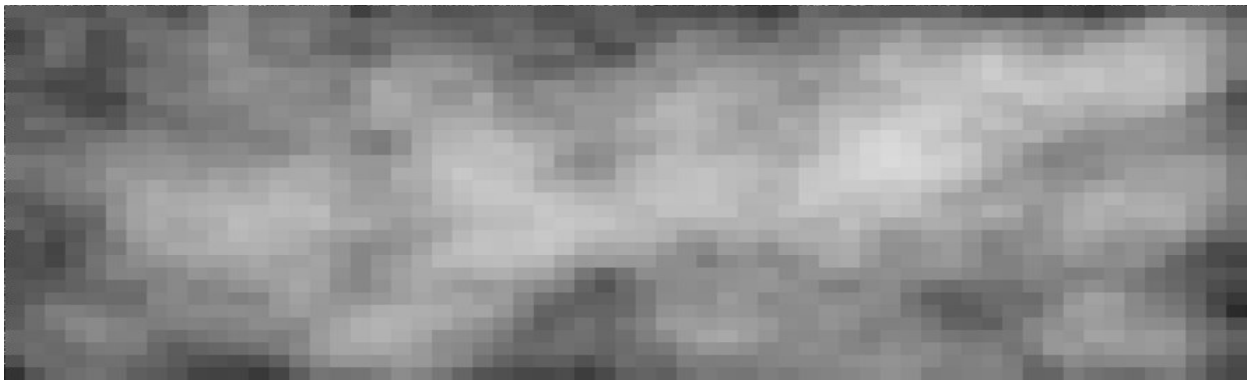

Figure 1. A grayscale pixel image used to simulate the damage on gray iron pipes as a replacement/ substitution for actual physical data.

2.1.2 Electrical Power Research Institute-Based Data

Using the EPRI laser scan data, similar approaches to those described previously were followed. The EPRI data representing the cylindrical coordinates and the corresponding depth after removal of degraded material were given in an Excel spreadsheet. The data were converted into a comma-separated value text format that could be utilized by a MOOSE function object to facilitate a 2-D piecewise linear interpolation of gridded data. The data were mapped onto the cylindrical pipe surface and employed the displacement boundary condition and diffusion procedure to obtain a final mesh with the sandblasted volumes removed, as shown in Figure 2.

A closer examination of the mesh geometry obtained by the boundary condition and diffusion procedure where the function representing the relative heights is used to solve a diffusion problem revealed some unsatisfactory local mesh distortions in elements near the surface. Using Paraview, [4] the mesh can be further examined near crevices, as seen in Figure 3. The stresses and strains are too "compressed" on the mesh due to the manner in which the layers and mesh elements are created. The deformation is locally concentrated nearest the surface instead of being distributed inward radially from the irregularities.

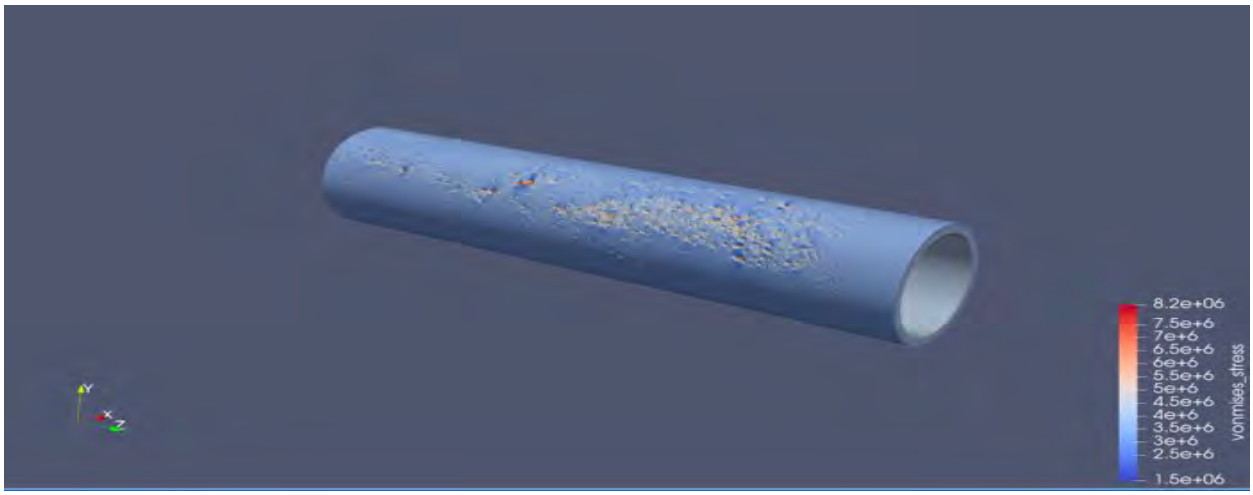

Figure 2. Pipe showing von Misses stress for internal pressure of 655E3 Pa. The diffusion method described above was followed to produce the changes in elevation on which the mechanical stresses and strains could be evaluated.

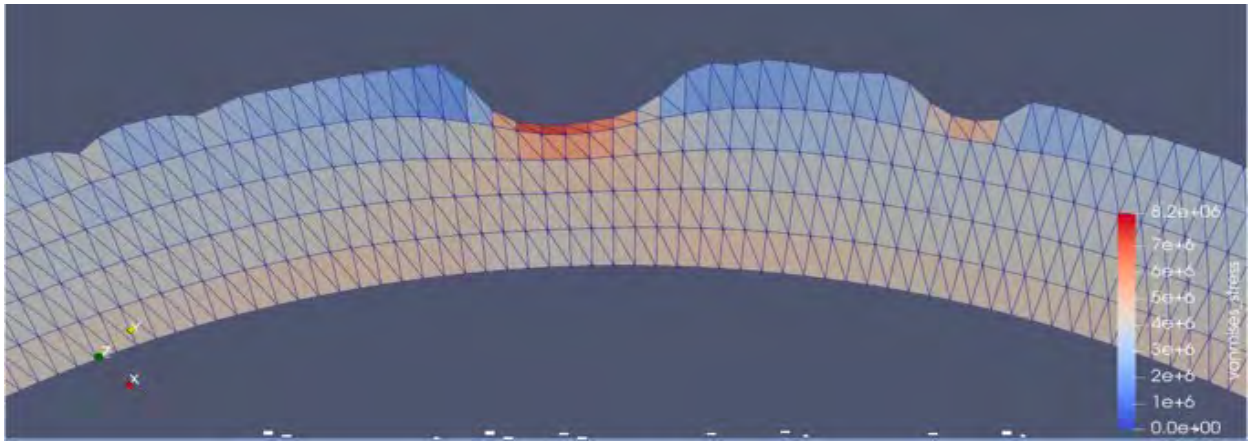

Figure 3. The method of using the solution of a diffusion through boundary conditions of the elevation map from EPRI data or PNG images. Note: The surface effects cause the layers to only be distorted near the outer surface instead of distributing the asymmetry inward radially.

A second method was developed to refine the layers by explicitly translating all interior nodes radially to the elevation profile from the laser scan data. A function and a new class were created that mapped the change in the surface to readjustments in the layer position accordingly. This gives a more refined layer spacing (Figure 4 and Figure 5), and in turn, a less “squeezed” representation of the strains and stresses.

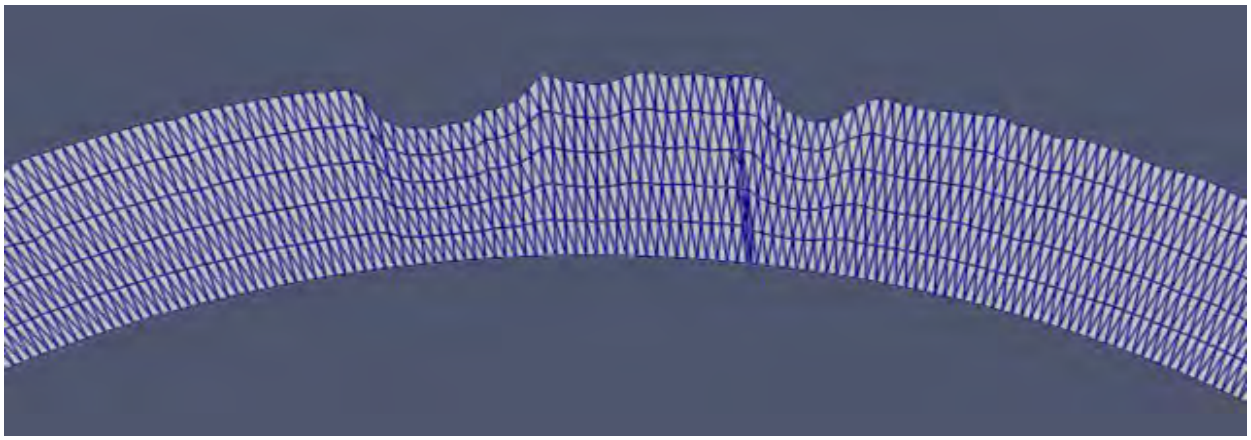

Figure 4. A refined mesh method to move evenly distribute the layer spacing. Note: This focuses on the spacing and does not display the strains.

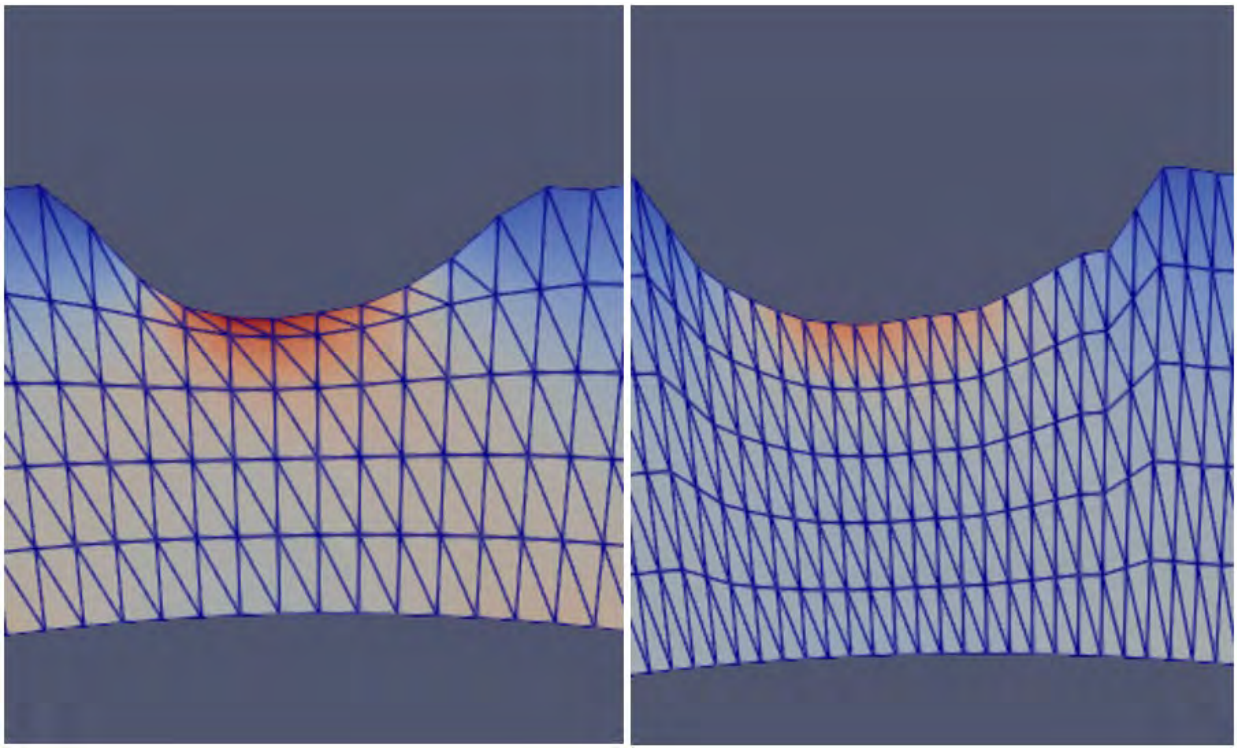

Figure 5. Showing the difference in the mesh refinement. The left-hand side is without changes in the node positions while the right side is with nodal refinement.

While the method of moving the mesh nodes gives an accurate distribution of the stresses and strains, it lacks the representation of the degraded surface material. While this layer is thin, it occasionally acts as a protective element that should be considered in a full simulation. Additionally, access to these data allows for the time evolution of the selective leaching process to be accurately modeled. In the case of a graphite plug forming, pressure surges and water hammers can result in pipe failures. Having a method of simulating the changes over time in the pipe is critical to effectively modeling the selective leaching process.

2.2 Current Results

Currently, a third method called XFEM is being refined. This method creates a “cut” of a section of the outer surface from a damaged pipe (shown in Figure 6). This cut will allow the mesh to be split into two parts, representing the undamaged pipe and the degraded material before removal as a unit on which simulations can be done. Such an approach will allow for a realistic representation of the actual conditions the pipe experiences in situ and should give a smoother distribution of mesh layer spacing.

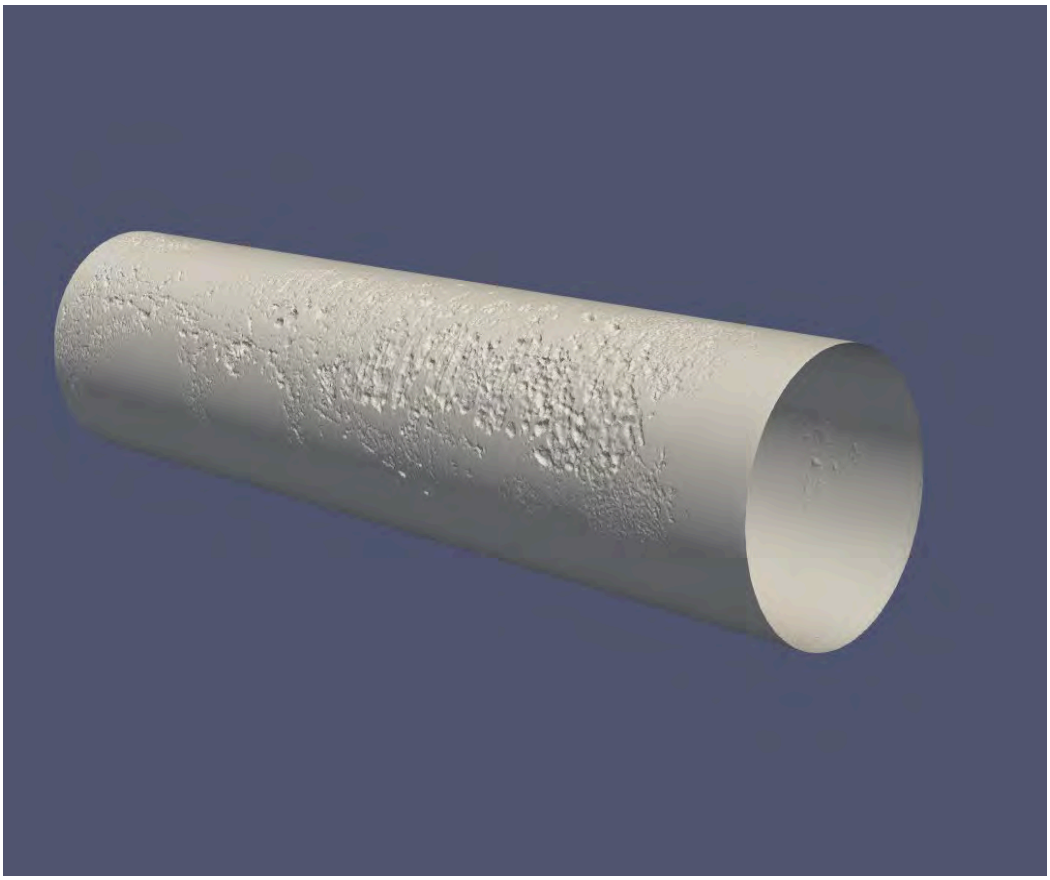

Figure 6. The “shell” mesh used to cut the un-displaced pipe mesh. This mesh is the outer surface area generated from the method described in the second implementation.

The truest to life representation of the effects of graphitic corrosion are demonstrated using XFEM. The thin surface layer of graphite matrix that seems visually normal can either aid or hinder the pipe performance, and it is most accurately modeled using XFEM. As shown in Figure 7, pitting and surface effects of selective leaching are accurately rendered into a mesh without the distortion found in previous approaches. Different material properties can be applied to the separate, but connected meshes, which most accurately describe the physics being considered for failure.

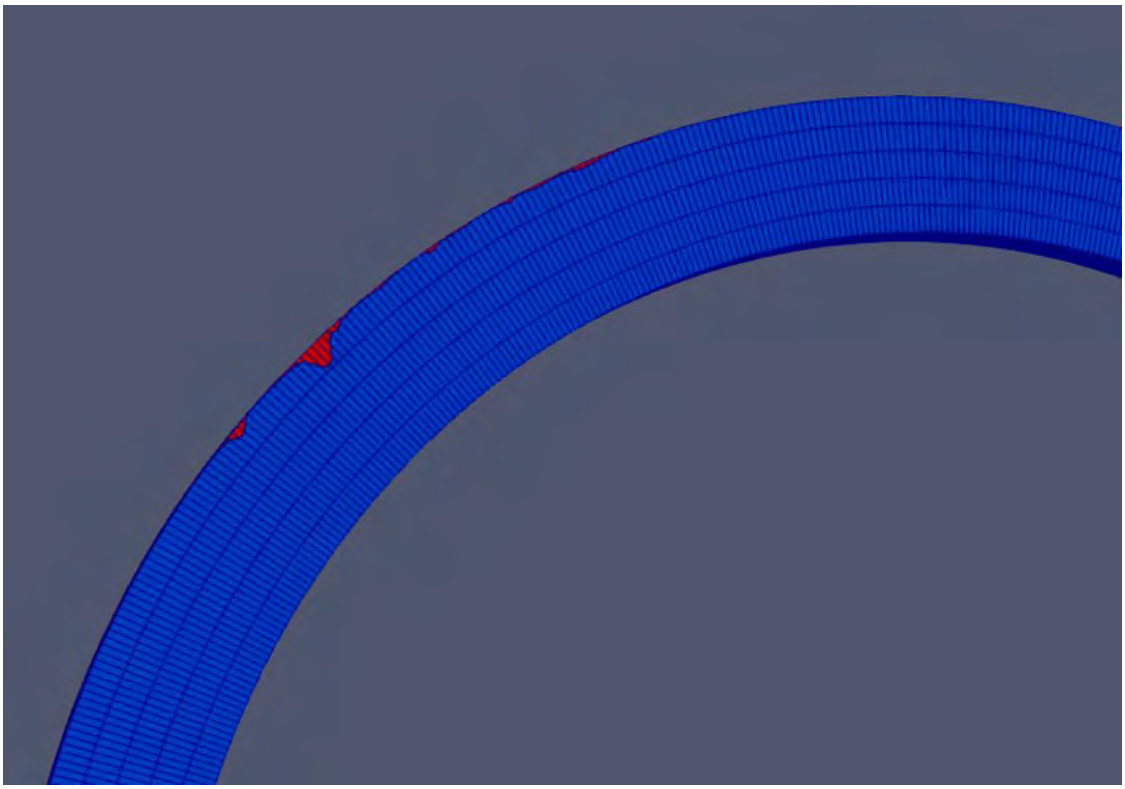

Figure 7. An XFEM cut that separates the undeformed pipe (blue) from the graphite shell (red).

Two cutting methods are applicable in the XFEM module, specifically cutting via a shell mesh and level set. The former involves creating a "shell" mesh of the cutting surface, while the latter is used to represent the geometry of the interface implicitly, usually using a signed distance function. The shell mesh method can be directly applied from laser scan data, making it relatively easy to apply. However, this method is the most computationally expensive and it currently takes an excessive amount of time to run. Using the level set method does involve creating a function to map the laser scan data, but it is quicker and less computationally expensive. A way to speed up both methods is being investigated.

2.3 Path Forward

2.3.1 Immediate Plans

The immediate future work plans will focus on refining the XFEM method and developing a method to model the fracture probability. The XFEM scaffolding used thus far is superior in its ability to accurately model both the remaining GCI as well as the deteriorated material. The foremost weakness of long simulation times is primarily due to shortcomings in the algorithm used to cut the mesh. An investigation into refining this code is underway and is already showing promising results.

While a framework on solving the strains and stresses has been developed based on the information given, additional data sets can expand the simulation sets and confidence in the results. Existing MOOSE capabilities stresses and strains can be modeled on similar pipes. More synthetic data as described previously can be generated, either by generative artificial intelligence (AI) or manual methods. However, without additional data sets it is possible to misrepresent the physical conditions that would occur in the processes being studied. It is expected that Oak Ridge National Laboratory (ORNL) will complete an exploration on decay rates with a laser scan data set in tandem in FY-24. These results, in conjunction with additional data sets can expand the simulation sets and confidence in the results.

MOOSE can calculate failure probabilities using a three-parameter Weibull distribution. Data and previous research already exist for three-point bending of GCI. [5] Using available literature data for the Weibull modulus and the linear elastic properties of GCI should allow for the calculation of the fracture probability as a function of internal pressure. In addition, three-point bending of actual material samples will be performed in the future to obtain a distribution of failure stresses which will validate the literature-based results.

2.3.2 Leveraging MOOSE

The numerous physics modules and applications based on the MOOSE framework comprise a rich software ecosystem ripe with opportunity for scope broadening in the selective leaching research. Many of the tools follow the open-source model of MOOSE and are widely available with extensive documentation and user support. While some apps are restricted, access for users can be granted through an application process at https://inl.gov/ncrc. The Nuclear Computational Resource Center oversees the distribution of protected software via private GitHub repositories. Some of the MOOSE-based physics modules that are applicable to the selective leaching work are highlighted below.

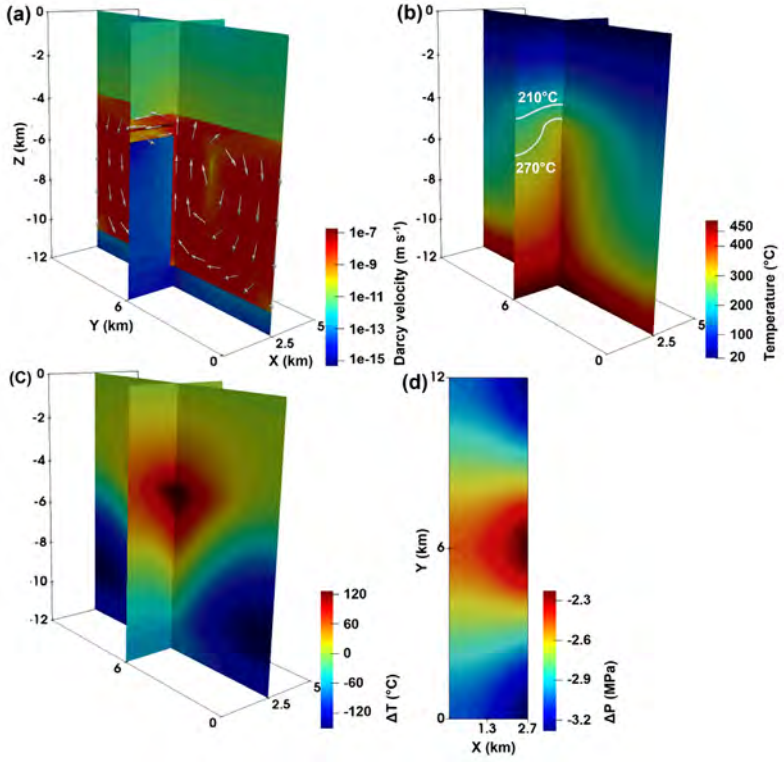

Figure 8. A large length-scale MOOSE-based porous flow model showing fluid transport, temperature, and pore pressure in permeable soil and rock matrix. From Yan et al. [6]

The porous flow module in MOOSE allows for rapid development of coupled thermal fluid flow in porous media, such as soil and permeable rock. Porous flow modeling has been successfully employed at INL in the context of geothermal systems and advanced reactor concepts. The MOOSE-based FALCON code is utilized for groundwater flow modeling and modeling of enhanced geothermal systems. The MOOSE-based Pronghorn app is a multidimensional, coarse-mesh, thermal-hydraulics code for advanced reactors and is typically utilized for modeling gas-cooled pebble bed and prismatic reactors. As such, this serves as an intermediate between detailed computational fluid dynamics analysis and lumped system models. A model for moisture transport in soil can be built using the components already present in the MOOSE ecosystem as shown by the example in Figure 8.

The MOOSE application Yellowjacket implements a Gibbs energy minimizer which can perform thermochemical equilibrium calculations for any material system for which a thermodynamic database is available. The chemical reactions module within MOOSE additionally provides a set of tools for the calculation of multicomponent aqueous reactive transport in porous media. In tandem, modeling corrosion processes such as galvanic, pitting, and general corrosion can be predicted. This method allows for corrosion to be predicted at the engineering scale and with varying chemical and electrochemical conditions.

The MOOSE phase field module provides tools to implement computational models based on the phase field method. Phase field simulations can be concurrently coupled with any physics modules available in MOOSE, creating a multiphysics modeling capability that includes mechanics and heat conduction, which can be obtained using the Tensor Mechanics and heat conduction modules. Mesoscale modeling can track the microstructure evolution of materials, such as cracks, grain structure, and local solute redistribution and depletion. This modeling capability enables predictive modeling of corrosion processes and their time dependence and in turn, ultimately, pipe failure. An example of work in this area is shown in Figure 9.

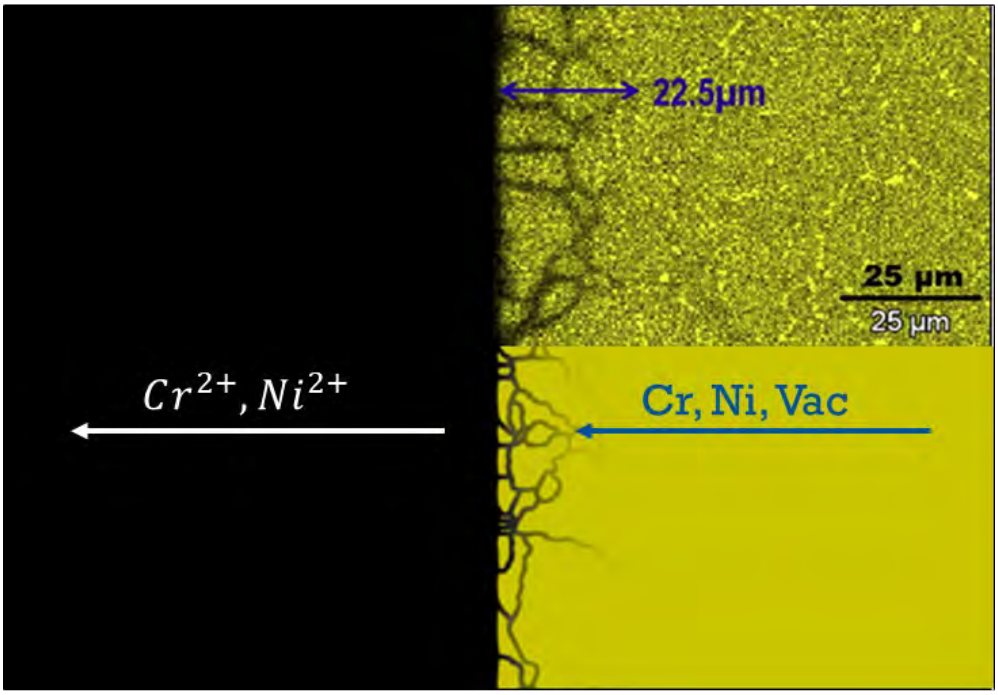

Figure 9. A MOOSE-based phase field simulation (bottom) of corrosion in an Incoloy (i.e., a range of alloys) surrogate system. Material microstructure influences the transport of alloy species with accelerated diffusion along grain boundaries. The top half shows the Cr signal from Energy-dispersive X-ray spectroscopy..

The stochastic tools module is a toolbox designed to assist with stochastic analysis for MOOSE-based applications. The module enables computing failure probabilities, rare event statistics, Bayesian inference for model parameterization from experimental or lower length-scale data, and uncertainty quantification. Sophisticated sampling strategies are provided with support for massively parallel Markov-chain Monte Carlo methods. Having a faithful representation of the physical processes in selective leaching and, in turn, reliable failure probabilities with quantified uncertainties, adds fidelity to the simulation results and allows for accurate predictions.

3. EVALUATION OF LEACHING SUSCEPTIBILITY IN METALLIC PIPES

The selective removal, otherwise known as leaching, of specific elements or components from metallic pipes has been identified as a recurring problem in pipes carrying a range of fluids. Most importantly for U.S. nuclear reactors, buried pipes carrying process water have been found to develop leaks due to corrosion on the outer surface. These pipes are generally fabricated from cast iron; whether gray cast iron (GCI) or ductile cast iron (DCI) depending on the fabrication process and prior heat treatment. Furthermore, many of these pipes have not been protected by a protective wrap or coating, or by a properly installed and operated cathodic protection system.

It is important to note that leaching is defined as the selective removal of an alloying element from the parent matrix which results in an apparent enrichment of the other elements that remain in the matrix. When dealing with aluminum bronze or a zinc-rich brass, selective removal of aluminum or zinc, respectively, meets the definition of leaching. Alloying elements in cast irons are present in considerably lower concentrations (~2–4% carbon and ~1–3% silicon) and sometimes with even smaller amounts of other alloying elements like manganese and nickel. Corrosion of cast iron pipes is characterized by formation of an iron-rich corrosion product where iron from the matrix reacts with components of an aggressive environment. The remaining unreacted metal will still primarily be iron although there might appear to be a slight enrichment of the minor alloying elements.

When exposed intermittently or continuously to moist soil, thermodynamics predict that unprotected iron pipes will corrode and form an iron oxide layer on the exposed surface. The rate of corrosion will be strongly affected by the properties of the soil—its chemical composition, its acidity, and the frequency of water saturation. In environments where chloride salt is regularly used for deicing, chloride-laden moisture reaching the pipe surface can accelerate corrosion of iron pipes.

Accurate prediction of the corrosion rate and even the failure rate of buried iron pipes is essential to operators and users of these buried pipe systems. Without excavation, first-hand inspection of the exposed outer surface of these pipes is not possible, and excavation of entire pipe systems is not a practical approach. When damaged pipe sections have to be replaced, the removed sections can be characterized by cleaning and then making profile measurements of the exposed surfaces. However, it has to be considered that the removed sections are examples of the worst damage that can occur and thus are not representative of the entire piping system.

That leads to the question as to how degradation and the rate of degradation of a buried cast iron pipe might be predicted. Laboratory corrosion studies can be used to determine what environmental components would accelerate pipe degradation, but it is a big challenge to determine how the degradation rate can be predicted based on laboratory studies.

3.1 Approach

The approach used for this project consists of three primary efforts. The first task consists of review of the literature on selective leaching of pipe components. The relevant data were collected from the reports provided by EPRI as well as identified open literature reports.

Another task is to thoroughly examine and then assess the nature and extent of degradation of pipes, primarily cast iron, which have been exposed to corrosive environments for extended times. Identification of the corrosion products will aid in determining the degradation mechanism, and defining the extent of corrosion will aid in predicting lifetimes.

The third task consists of laboratory exposures of selected alloys, GCI and DCI for this portion of the study, to selected aqueous-based environments. These environments are selected to produce, in accelerated manner, degradation of the selected alloys which is comparable to that seen after long term

exposure. For future studies, the alloys to be studied will include the two cast irons, for further investigation, as well as two copper base alloys, which was not used for the lab study in this report.

3.2 Literature Review

The material provided included eight EPRI reports on detection, control, and prevention of leaching as well as a list of ten open literature publications, seven of which we were able to acquire and review. [7–13] These seven papers concentrated on the fracture and fatigue properties of cast iron pipes. Reference [7] investigated the strength and deformation properties of cast iron water mains. These properties were determined from coupons extracted from exhumed water mains. They found the cast iron materials showed negligible plastic strain at a stress less than 75 MPa.

For the second reference, researchers in Australia showed the major factors contributing to longitudinal failures in large diameter (≥300 mm) cast iron water pipes are corrosion and internal water pressure. Their studies showed fatigue-initiated cracks at critically corroded areas. The third reference reported on an investigation of the stress concentration factors of isolated elliptical corrosion pits which could reduce pipe resistance and lead to pipe breakage by intensifying the local stress field. Reference [10] describes a study of the propagation of fatigue cracks in samples of different types of cast iron to investigate the role of the microstructure on the fatigue behavior of cast iron trunk mains. This study demonstrated that the fracture toughness and fatigue behavior of cast iron used in the water industry shows a range of behavior dependent on the details of the microstructure. The fifth reference notes that pipe lifetimes can be over-estimated if remaining wall thickness is used as the criteria. This paper takes into consideration the loss-of-section aspect as a consequence of pitting and adds a fracture mechanics analysis which considers geometric and loading conditions. Reference [12] by Ugoh et al. notes that waste water trunk sewers are typically exposed to harsher and more complex internal and external environments. Cast iron sewer pipes can experience significant internal surface pitting, and this study provided a revised model to account for corrosion pitting on the internal surface. In the seventh reference, Mohebbi et al. [13] reported on their study of fatigue crack propagation in GCI water pipes. They found clear differences in fatigue crack behavior in samples from different pipes, and they determined that microstructural differences played a role in mechanical behavior.

References [14–16] are EPRI reports that more specifically address the issues and approach to solutions for piping used in nuclear reactors. The first of these references, EPRI Report 3002013156 is divided into two sections; integrity evaluation and repairs. The first section "…provides engineering guidance for the evaluation of the integrity of degraded or nonconforming piping systems," while the second section covers the various pipe repair techniques. [14] EPRI Report 3002020713 "…presents the framework piloted on selective leaching and cable AMPs (Aging Management Programs) to ensure that the focus is on those activities that are more significant while reducing focus on less valuable activities." [15] The third of these reports addresses the phenomenon of selective leaching or preferential dissolution for four alloys of particular interest to commercial NPPs. [16] The mechanisms of selective leaching are summarized and results of limited laboratory studies are presented with the goal of better understanding the metallurgical and environmental factors affecting the susceptibility of the alloys of interest to selective leaching.

In addition, to the papers and reports in references [7–16] suggested or provided by EPRI, a literature search identified a large number of documents on cast iron. A number of relevant publications were identified and reviewed. These include references [17–22]. The first of these references is over 50 years old and addresses the performance of the newly introduced DCI pipes compared to the traditional GCI pipes. The observation is that the DCI material, in terms of corrosion resistance, is at least as good as the traditionally used GCI. A paper from over 25 years ago [18] by B. Rajani et al. describes a model which was developed to simulate the responses of a jointed cast iron water main subjected to differential temperature changes, changes in water pressure and axial and radial restraints offered by the surrounding soil. Reference [19] is by a researcher, J.M. Makar, who, like Rajani, has published a number of papers addressing issues with cast iron. This particular paper describes the four common failure modes seen in GCI water pipes. Jesson et al. [20] considered the effect of microstructure and in-service corrosion (graphitization) and found that the degree of graphitization influences the residual strength. In reference [21], G. Cilluffo provided an approach for establishing an internal corrosion rate after a first-time inspection utilizing actual plant-wide piping inspection data, leak history, repair history, and corrosion monitoring results.

Reference [22] is a fairly recent publication describing an effort to determine what mitigation strategies would be required to enable ductile iron pipe to survive for 50–100 years. The project addressed zinc-coated, polyethylene encased and cathodically protected pipes. It was concluded that the database was too limited but indications were. "…that combinations of these strategies could be very effective in protecting ductile iron pipe in corrosive soils." Reference [23] describes the examination of failed water pipes removed from service at ORNL. Extensive corrosion was observed with through-wall corrosion found in many places, even some where the corrosion product was the only thing blocking the apparent leak path.

3.3 Pipe Examinations

We were not able to obtain any pipe sections from nuclear reactor sites. We were provided with a check valve (Figure 10) which was sectioned per our request, and we examined pieces of the check valve which had been exposed to a process water environment. We, fortuitously, had been asked to examine sections of failed cast iron water pipes which had been buried on the ORNL site for many decades (see Figure 11), and this provided us with pipe sections which we could examine to get an indication of the failure mechanism. We also obtained pieces of cast iron pipes used for transporting air and water on the ORNL site and which had been in a concrete vault that was expected to protect the pipes from the environment.

Figure 10. Pieces of cast iron check valve provided by EPRI for examination of areas exposed to the process fluid. [7]

Figure 11. Failed cast iron pipes from ORNL water lines. [8]

3.4 Laboratory Studies

Pieces of GCI and DCI were cut from 2-inch-diameter bars. These were quartered to provide manageable pieces with curved surfaces to simulate the outer surface of a pipe. Tests were conducted by exposing limited areas of these samples (see Figure 12a) to selected aqueous solutions, as summarized in Table 2, to determine whether corrosion could be produced that was comparable to what was seen on pipes exposed to corrosive environments for extended times. Two DCI samples after 1000-hour exposure in two corrosive solutions are shown in Figure 12b as examples. Also, anodic polarization of a GCI sample was performed to see if this could form a representative surface attack and corrosion product. To evaluate the corrosion product, samples were sectioned and examined using light microscopy and the scanning electron microscope with an EDS attachment for determination of the elemental distribution in the samples.

Table 2. Summary of laboratory accelerated corrosion tests for gray and DCI samples.

Corrosive media	0.1 M NaCl	0.1 M NaCl 0.05 M Na2SO4	0.1 M NaCl 0.001 M H_2SO_4	0.1 M NaCl 0.05 M Na2SO4 0.001 M H_2SO_4	3.5% NaCl 0.05 M Na2SO4 0.001 M H_2SO_4
Solution pH	6~7	6~7	~3	~3	~3
Immersion test time (t) & anodic polarization condition	t = 200 h	t = 200 h	t = 200, 500 & 1000 h	t = 200, 500 & 1000 h	anodic polarization at Ecorr[1] + 800 mV or + 300 mV

[1] E_{corr} – corrosion potential

3.5 Results

3.5.1 Component Examinations

For the check valve, the inner surface of the flange was identified as having been exposed to the process fluid which was likely to have been “raw” water. This water could have come from rivers, lakes, or wells and would have been untreated, but information on the source of the water was not available, so the water could have been treated or untreated. The section of the flange shown in Figure 13 was cut to remove pieces 4 and 5 (#4 and #5), and metallography samples were prepared from the corroded areas shown in the white ovals. In Figure 14, cross-sectional light microscopy images from #4 and #5 are presented. In the uncorroded substrate, dispersion of graphite flakes indicates that the valve section was GCI. The deeper corrosion growth is shown along the graphite flakes, which is typical graphitic corrosion. To assess corrosion depth statistically, eight depth measurements were made from the #4 and #5 samples as shown in Figure 15. The average of eight depths is 1212 micrometers (μm) with standard deviation of 674 μm. According to the service history provided by EPRI, the valve’s internal surface was exposed to an unidentified cooling water for 12 years. Assuming linear growth of corrosion depth, the average corrosion rate can be estimated as 100 μm per year or 274 nanometers per day. An accelerated corrosion rate of 5.5 μm per day or 38.5 μm per week, which is about 20 times of the rate estimated in the check valves, can be considered as a reasonable target for an accelerated corrosion test. The corrosion rates from accelerated lab tests, discussed in the next section, were greater than the target value in certain cases.

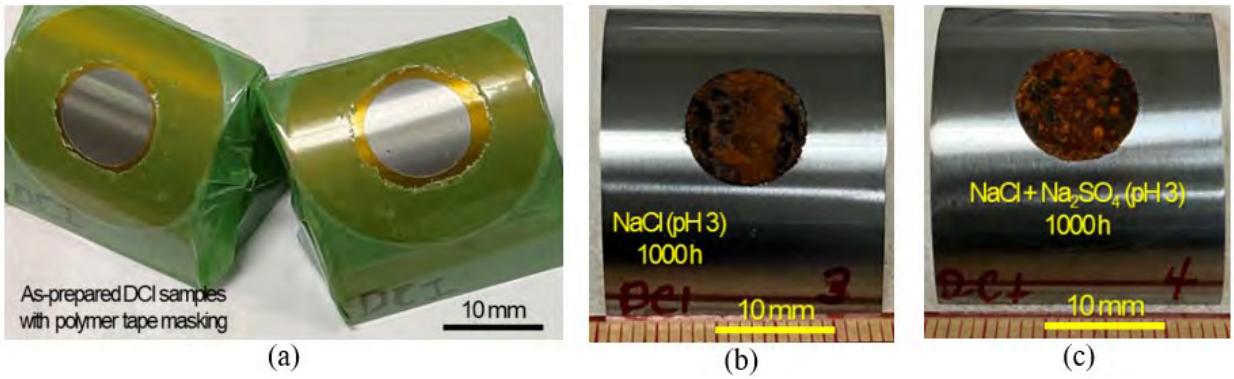

Figure 12. (a) Example of two DCI samples prepared by cutting a disk from a 2-inch-diameter bar and then cutting the disk into four pieces. Tape was applied to limit the area that would be exposed to the corrosive environment. (b, c) The post-exposure DCI samples with corroded area from 0.1 M NaCl (pH 3) and 0.1 M NaCl + 0.05 M Na2SO4 (pH 3) immersion for 1000 h.

The two process water pipes shown in Figure 11 were replaced when leaks developed after decades of service buried in the acidic clay soil of East Tennessee. Examination of metallographic samples from the two pipes showed they had the characteristic microstructure of GCI as shown in Figure 16. Elemental maps of a typical surface layer obtained using energy dispersive x-ray spectroscopy are presented in Figure 17 and show the corrosion product is an iron oxide. To collect information about the failure mechanism, several rings were cut from one of the pipe samples with the plan to collect metallography samples from a severely thinned area. However, examination of the rings showed that extensive corrosion originating on the outer diameter had occurred in many locations that were revealed when the ring sections were cut. Figure 18 shows photos of several of the cross-section rings, and it is apparent that some areas had only minimal corrosion attack while severe wall thinning occurred in many locations. The retention of the oxide corrosion product gave the outward appearance that the pipe was not significantly corroded in many areas, but these cross sections show the retained corrosion product only made it appear that the pipeline was intact in most areas. As noted by the red arrows, there are many areas on these pipe sections where there is little or no remaining metal.

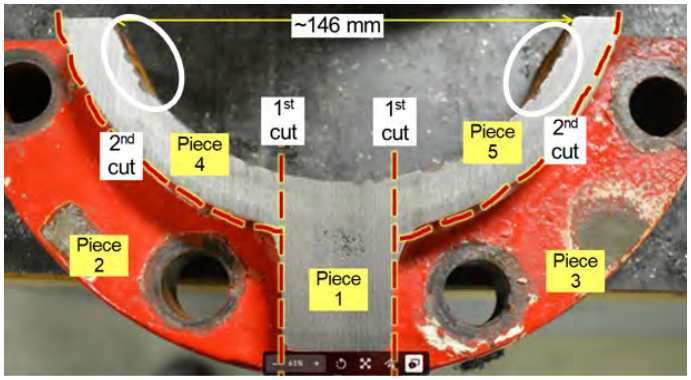

Figure 13. The white ovals identify the areas where metallography samples were collected. Light micrographs of these samples in Figure 14 show the material is GCI, a significant layer of corrosion product is present on both samples, the corrosion sometimes follows the carbon platelets, and the corrosion product contains many cracks.

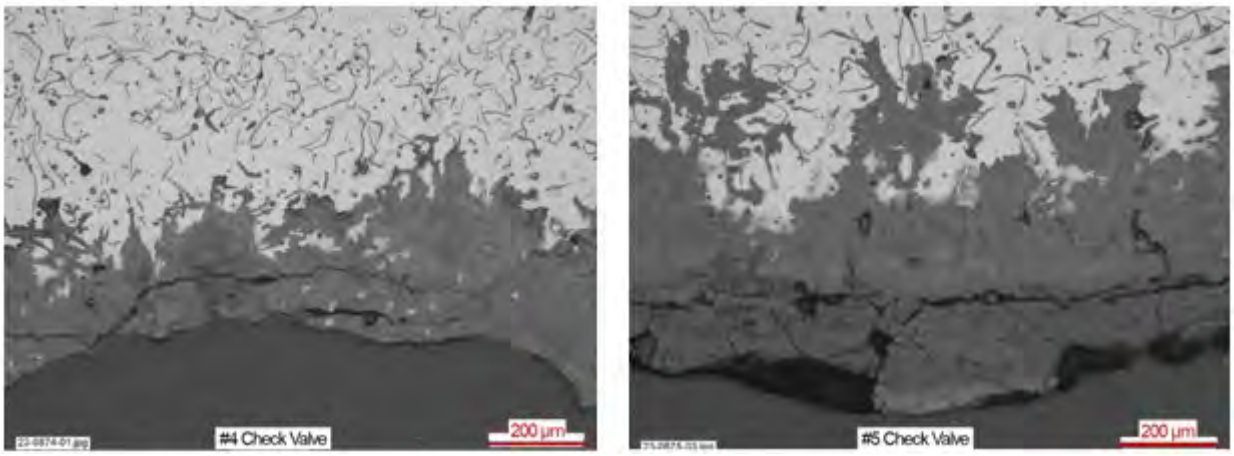

Figure 14. Light micrographs of cross sections of pieces cut from Sections #4 and #5 of the check valve show the material is GCI and there is a significant corrosion product which, based on the cracking, is likely susceptible to spalling of the corrosion product.

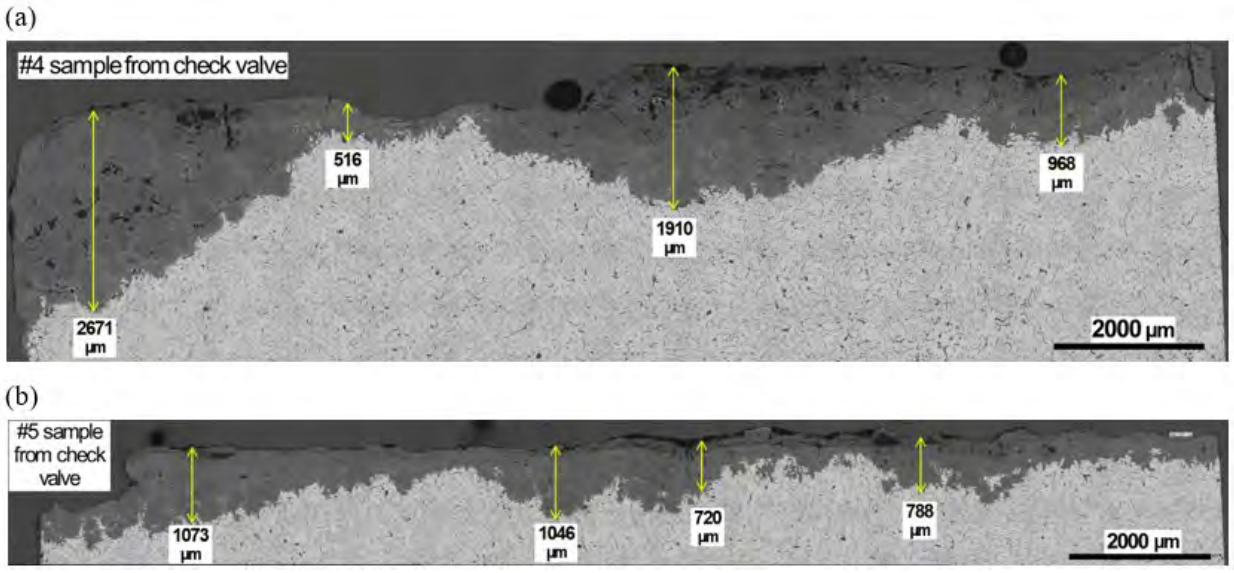

Figure 15. Light micrographs of cross sections of samples cut from Sections #4 and #5 of the check valve showing measurements of the extent of material lost to corrosion.

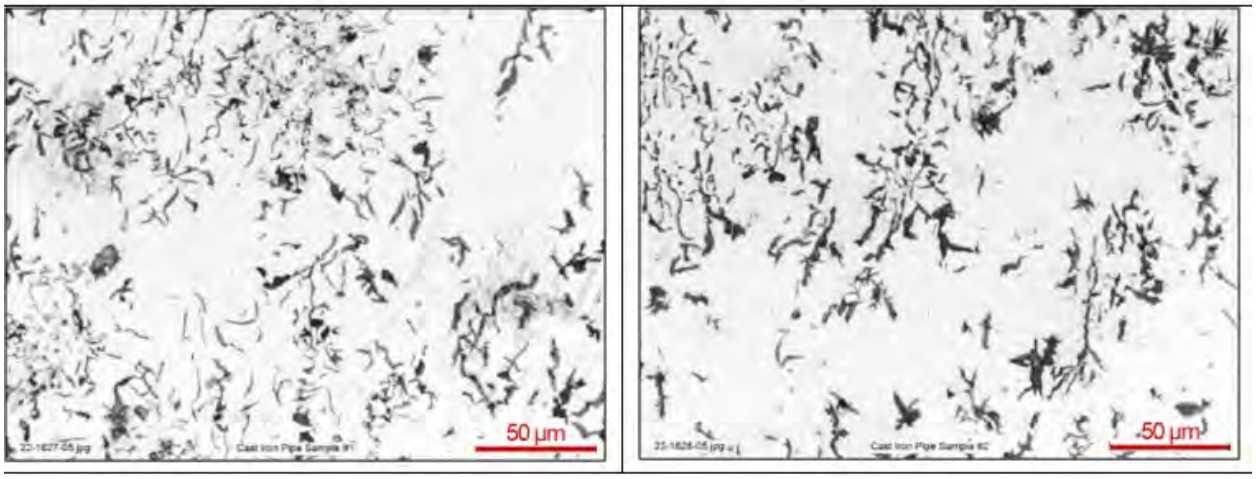

Figure 16. Light micrograph of typical areas of the two sections of the ORNL water pipes showing a microstructure typical of GCI.

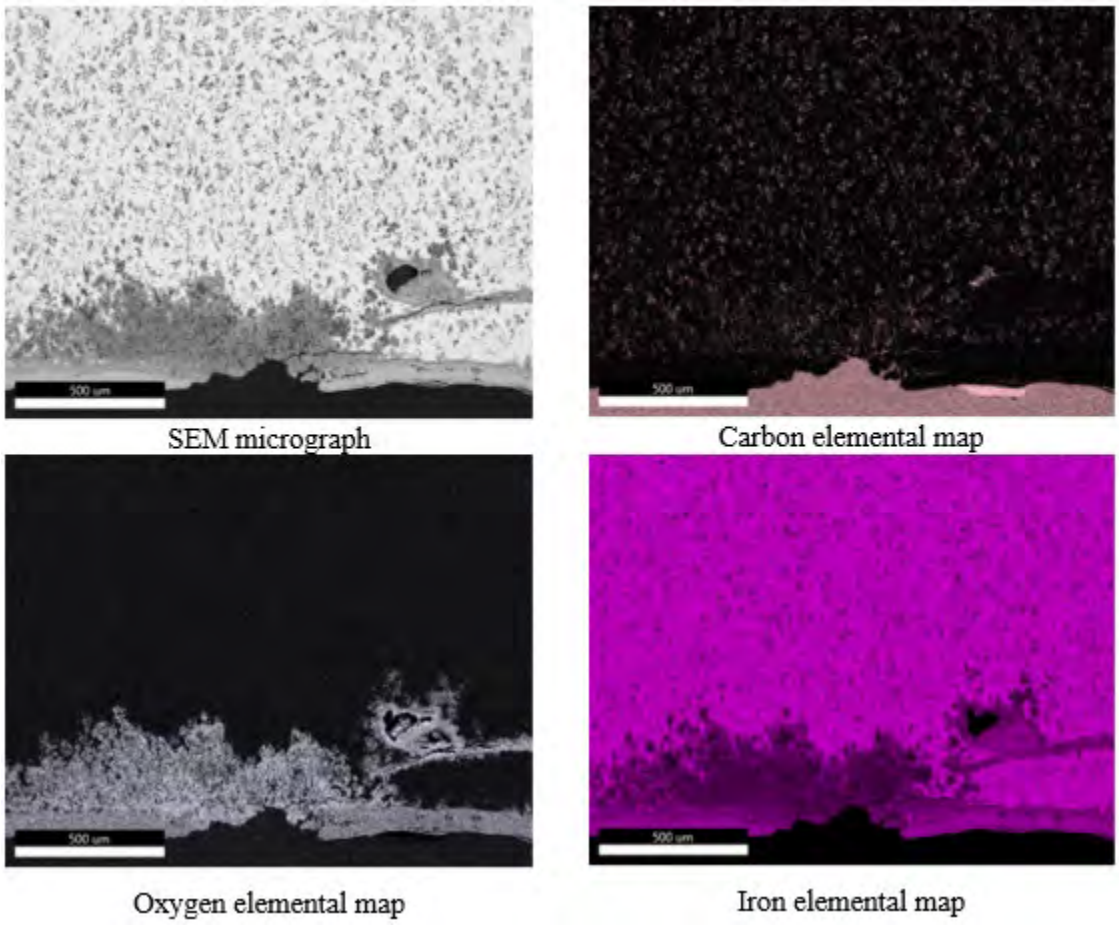

Figure 17. SEM micrograph and EDS elemental maps confirm the corrosion product on the surface of the sample is an iron oxide. For the elemental maps, the lighter the shading, the higher the concentration.

Figure 18. Photos of cross sections of the rings cut from the corroded cast iron pipe. Shiny areas are unaffected metal while the dark areas are the oxide corrosion product. Photos show areas of significant corrosion. In the bottom photo note the area of through-wall corrosion on the far left side.

The ORNL pipes used for air and water transport were in a concrete vault which was expected to protect them from the environment. The top cover of the vault consisted of concrete plates which also served as sidewalks. During the infrequent periods of snowy or icy weather, deicing salt was applied to the sidewalks. Unfortunately, water containing dissolved salt seeped through the joints between the concrete plates onto the top of the pipes in the vault. Consequently, the salt-containing electrolyte resulted in corrosion on the top side of the pipes, and eventually, failure of the pipes. Figure 19a and Figure 19b show cross-section micrographs of the corrosion attack on the outer and inner diameter of an ORNL water pipe. The maximum corrosion depths in these specific OD and ID locations are 1444 and 178 μm, respectively. Full penetration of the pipe occurred about 10 centimeters (cm) from the area shown in the micrograph. This observation confirms the fact that the occasional exposure of the OD to water containing deicing salt caused greater corrosion depth. The ORNL water pipe was used for about 30 years before its removal, and the assumption of linear corrosion growth at this specific location gives the estimated corrosion rate of 48 μm per year or 0.13 μm per day. This rate is about 50% of the rate estimated from the average ID corrosion attack of the check valve shown in Figure 14 and Figure 15. For a location with full penetration of the pipe, the corrosion rate was at least 0.21 mm/year or 0.58 μm/day which is about 10% of the targeted accelerated rate.

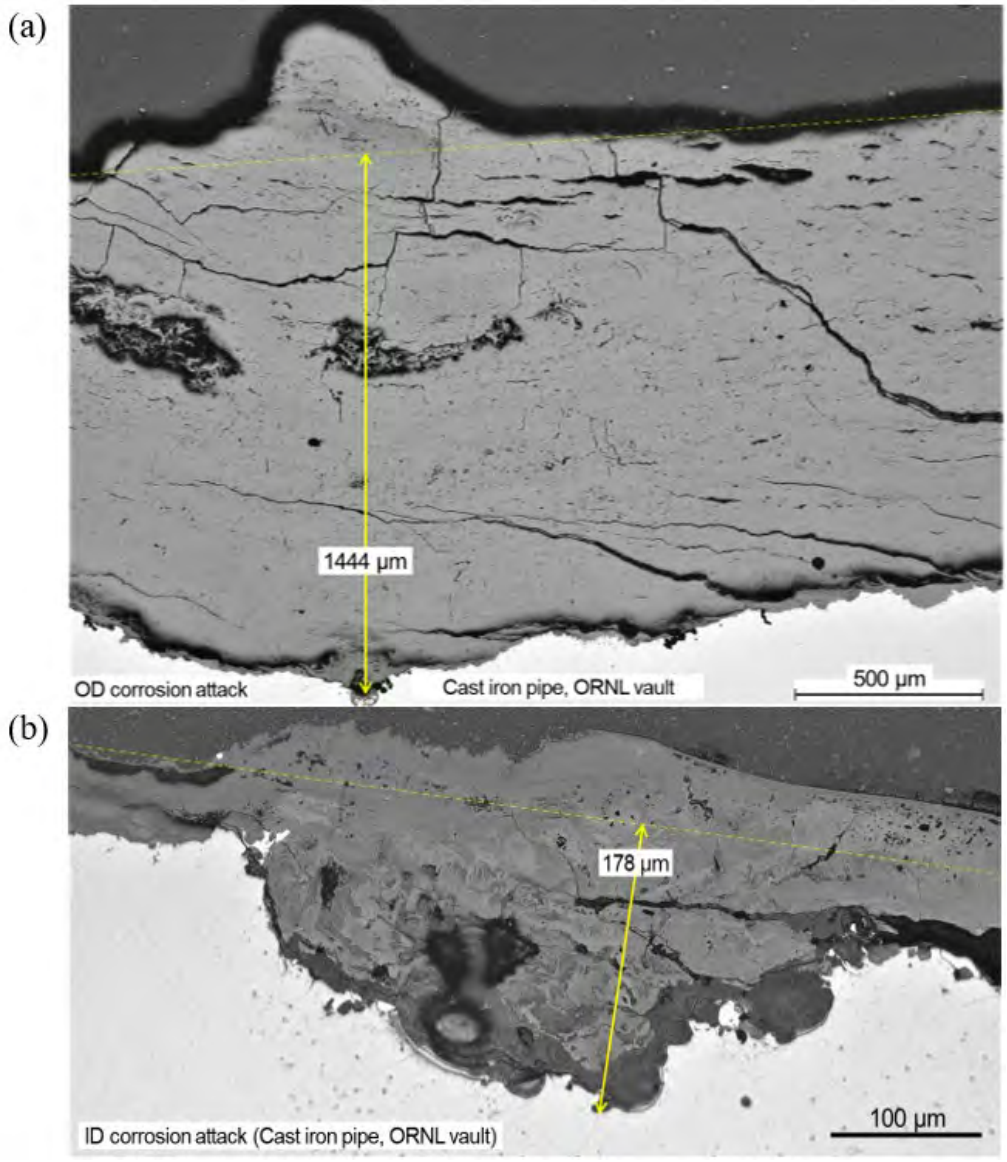

Figure 19. Optical microscopic images of (a) OD and (b) ID corrosion attacks in ORNL vault cast iron pipe in cross-sectional view.

3.5.2 Laboratory Studies

Figure 20a shows the cross sections of GCI and DCI samples after 200 h immersion in two neutral corrosive solutions, 0.1 M NaCl and 0.1 M NaCl + 0.05 M Na_2SO_4. Localized corrosion attack, including dish and semi-circular shape pits, is observed on the samples after 0.1 M NaCl exposure, while relatively continuous corrosion layers were seen in the samples after exposure in 0.1 M NaCl + 0.05 M Na_2SO_4. To determine the maximum corrosion depths, several light microscopy images within the observed cross sections were analyzed, and the results are compared in Figure 20b. For 200 h immersion in neutral corrosive solutions, GCI showed greater corrosion depth than DCI. The corrosion depth of localized attack after 0.1 M NaCl exposure was greater than the depth of the continuous corrosion layer after 0.1 M NaCl + 0.05 M Na_2SO_4 for both DCI and GCI. As typical metallic pipe degradation after field service is mostly associated with the formation of a continuous corrosion product layer, it can be said that 0.1 M NaCl + 0.05 M Na_2SO_4 exposure produced field exposure relevant corrosion attack for the cast iron samples. Based on the maximum depths in GCI and DCI (17 and 10 µm), the corrosion rates are calculated as 2 µm and 1.2 µm per day. These values are smaller than the target rate, 5.5 µm per day, thereby the neutral corrosive solutions are not considered sufficiently aggressive. For this reason, the pH of the two solutions was lowered to 3 by adding sulfuric acid (H_2SO_4) to produce a more corrosive solution.

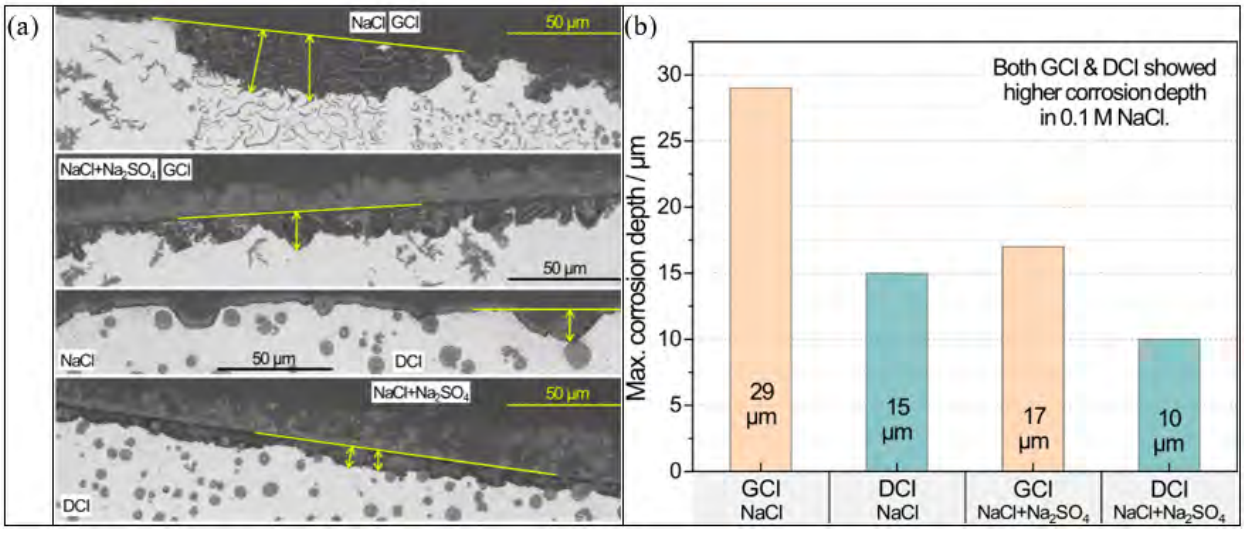

Figure 20. a) Micrographs of cross sections of GCI (top two micrographs) showing extent of corrosion in NaCl and NaCl + Na_2SO_4 solutions and DCI (bottom two micrographs) exposed to the same solutions and b) plot of maximum corrosion depth of the two materials in the two solutions.

Figure 21, Figure 22, and Figure 23 show cross sections of GCI and DCI exposed to the two acidic (pH 3, adjusted by 0.001 M H_2SO_4) solutions, one containing 0.1 M NaCl and another containing 0.1 M NaCl + 0.05 M Na_2SO_4, along with corrosion depth measurements designated by two-way arrows. After 200 h immersion (Figure 21), pitting attack was prominent in GCI samples while relatively continuous corrosion attack was observed in DCI samples. After 500 and 1000 h immersion tests (Figure 22 and Figure 23), both GCI and DCI exhibited continuous corrosion attack that was deeper than the attack identified in 200 h exposed cast iron sample.

To quantitively compare the degree of accelerated corrosion attack, Figure 24 provides a graphical display of the maximum corrosion depths measured for the two materials in the two different solutions as a function of exposure time. Regarding the material type, GCI samples developed deeper corrosion attack than DCI samples in the two acidic solutions. For both GCI and DCI samples, the acidic solution (pH 3) 0.1 M NaCl + 0.05 M Na_2SO_4 caused higher corrosion depths than the solution without Na_2SO_4. The corrosion growth between 500 and 1000 h was higher than the growth between 200 and 500 h for all cases, indicating that the corrosion rates, associated with the observed maximum depths, were greater after 500 h immersion. Nonetheless, both GCI and DCI samples showed relatively linear corrosion growth, associated consistent corrosion rates, in acidic (pH 3) 0.1 M NaCl + 0.05 M Na_2SO_4 throughout the exposure to 1000 h.

In Figure 25, SEM and EDS characterization results are presented for both GCI and DCI samples after exposure in acidic (pH 3) 0.1 M NaCl + 0.05 M Na_2SO_4 for 500 h. The maximum corrosion depth, as designated in the SEM images, is greater in GCI than DCI, which agrees with the results presented in Figure 24. In EDS maps, the corrosion product layer of GCI based on ferrous oxides exhibited a Si en-riched area near the top and included carbon-rich phases. Meanwhile, corrosion attack in DCI appeared as major volume loss with Si- and O-enriched layer formed at the bottom. This is presumably because almost all solid silicon dioxide (SiO_2) remained while Fe was oxidized to form not only solid oxides (Fe_2O_3 and other iron oxides and hydroxides) but also aqueous Fe ionic species that were not present in the oxide. Further characterization of more corroded GCI and DCI samples will be useful to reveal the key mechanism which caused the observed corrosion features.

Based on the laboratory exposure results, the acidic solution with Na_2SO_4 is considered more suitable to produce accelerated corrosion attack as it resulted in deeper and almost linearly growing corrosion depths for both GCI and DCI samples. In the acidic solution NaCl + Na_2SO_4, the corrosion rates after 200-, 500-, and 1000-h immersions are approximately 6.5, 3.8, and 3.3 µm per day for GCI, and 3.9, 2.35, and 2.36 µm per day for DCI. Considering that the corrosion attack was not quite uniform after 200 h, it is reasonable that the corrosion rates for 500- and 1000-h immersion data, associated with continuous corrosion attack, are more practically relevant to the real-world degradation of cast iron pipes. The estimated corrosion rates of GCI and DCI, 3.3–3.8 and ~2.3 µm per day, respectively, are still lower than the target rate of 5.5 µm per day.

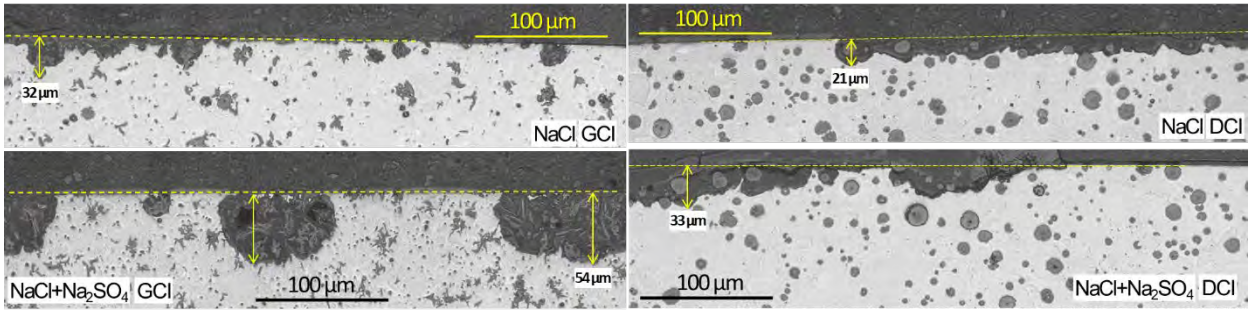

Figure 21. Micrographs showing depth measurements for the two cast irons in the two solutions with a pH of 3 after a 200-h exposure.

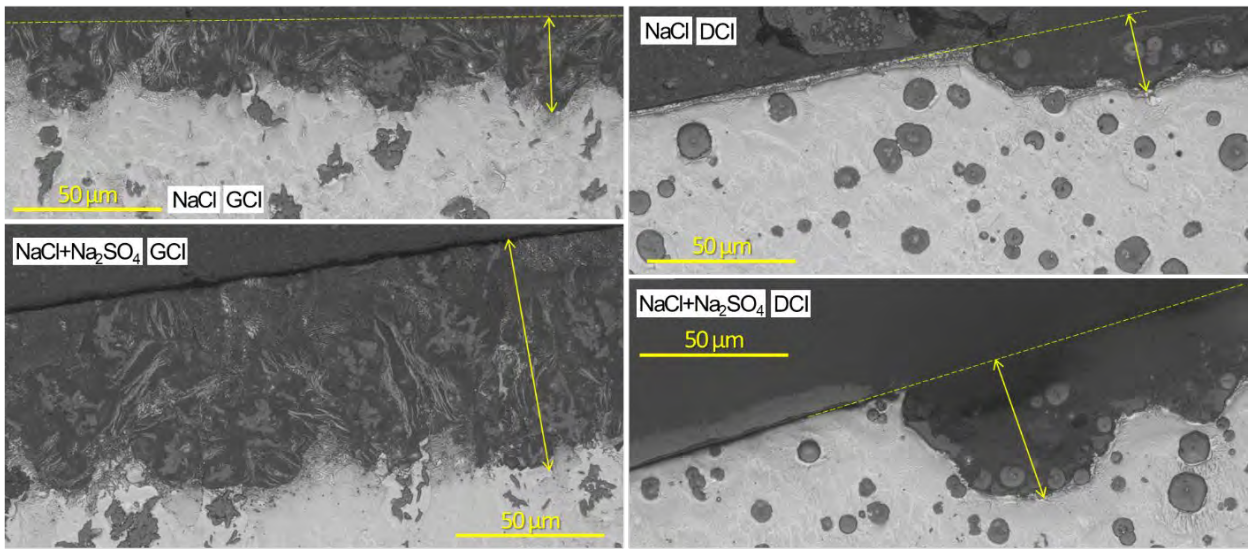

Figure 22. Micrographs showing depth measurements for the two cast irons in the two solutions with a pH of 3 after a 500-h exposure.

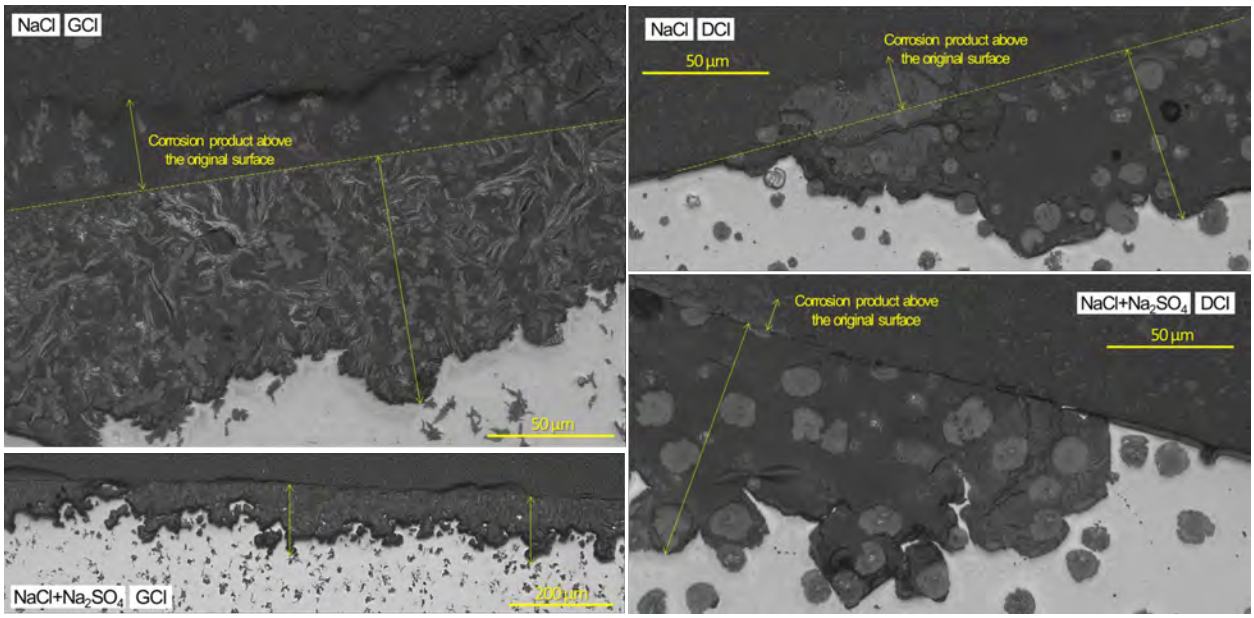

Figure 23. Micrographs showing depth measurements for the two cast irons in the two solutions with a pH of 3 after a 1000-h exposure.

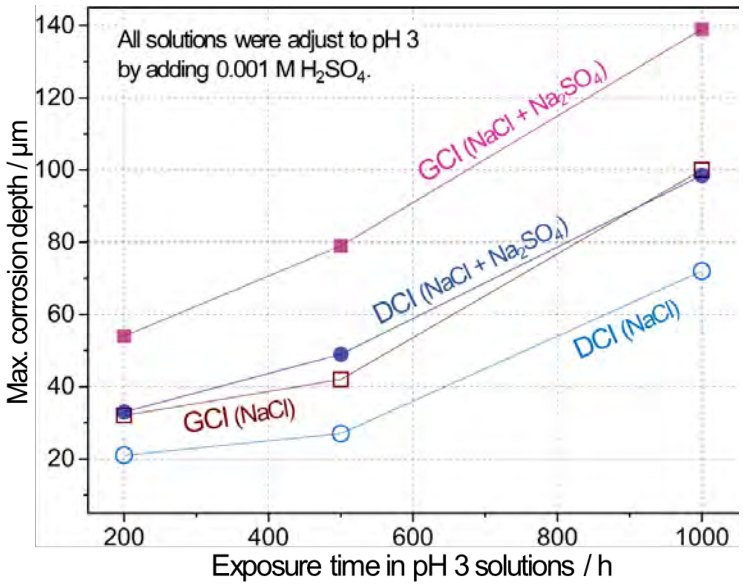

Figure 24. Plot showing maximum measured corrosion depth as a function of exposure time for GCI and DCI in the two solutions with addition of H_2SO_4 to reach a pH of 3.

To further increase the corrosion rates, anodic polarization was introduced for the cast iron samples in the acidic (pH 3) 3.5% NaCl + 0.05 M Na_2SO_4 solution. The three-electrode setup included a polymer tape-masked GCI sample, similar to the ones presented in Figure 12a, with a smaller exposure area of 0.124 cm^2 (⌀ = 4 mm), a reference saturated calomel electrode, and a graphite rod counter electrode with a significantly larger surface area than 0.124 cm^2. A photograph of the initial setup, where all electrodes are immersed in clear acidic (pH 3) NaCl + Na_2SO_4 solution is shown in Figure 26a. The GCI was polarized at 800 millivolt (mV) above the last measured corrosion potential (as previously presented in Table 2) for 22 hours per day. The polarization for 22 hours was repeated for 4 more days, making the total anodic polarization time 110 hours.

Nearing the completion of 110 hours anodic polarization, the solution containing the electrodes turned dark with significant solid precipitates on the solution surface and bottom, as shown in Figure 26b. This is because of the saturation of Fe ions, produced from anodic dissolution of GCI, in the solution. After the anodic polarization exposure for 110 hours, the GCI sample was visually inspected to preliminarily assess the degree of corrosion on the exposed area. A photograph of GCI sample after polarization is presented in Figure 26c where significant anodic dissolution occurred on the originally exposed area and along the adjacent area. It is also notable that some initially masked locations also exhibited corrosion loss. The observation of excessive anodic dissolution in GCI suggests that the applied potential, 800 mV above the corrosion potential, was overly intensive.

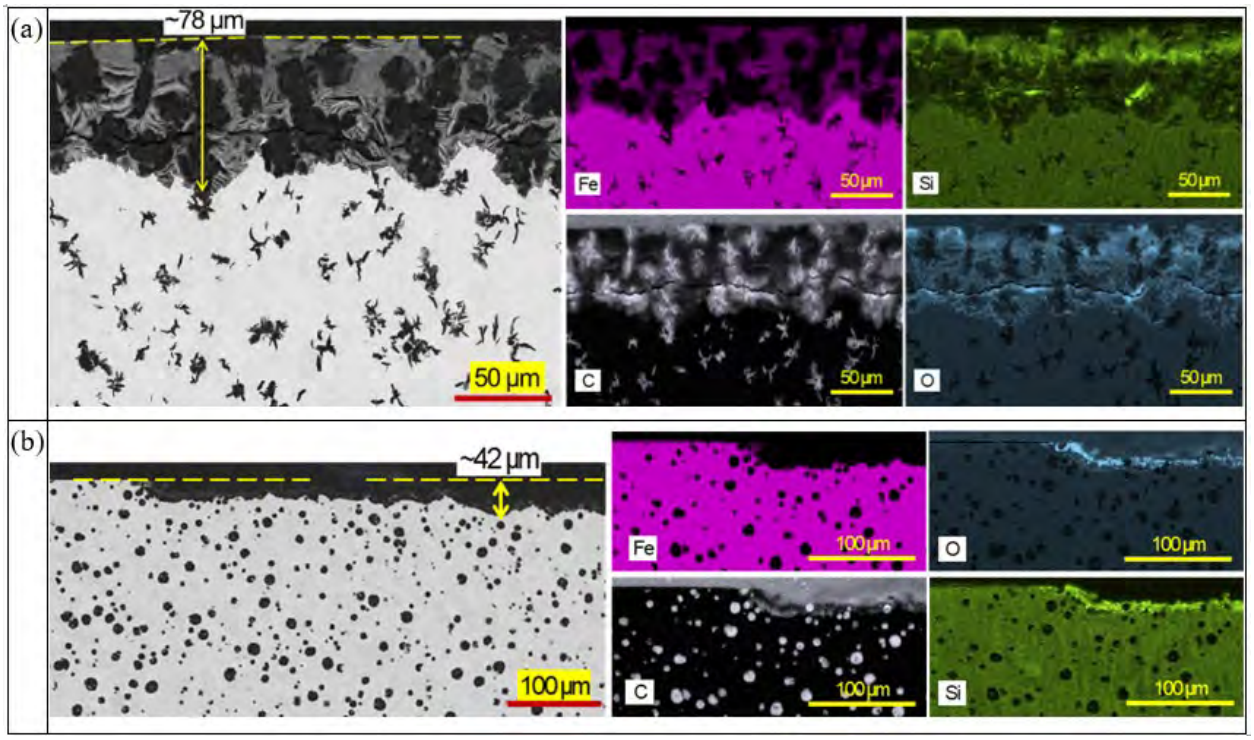

Figure 25. SEM images and EDS maps of (a) GCI and (b) DCI after exposure in pH3 0.1 M NaCl + 0.05 M Na_2SO_4 for 500 h.

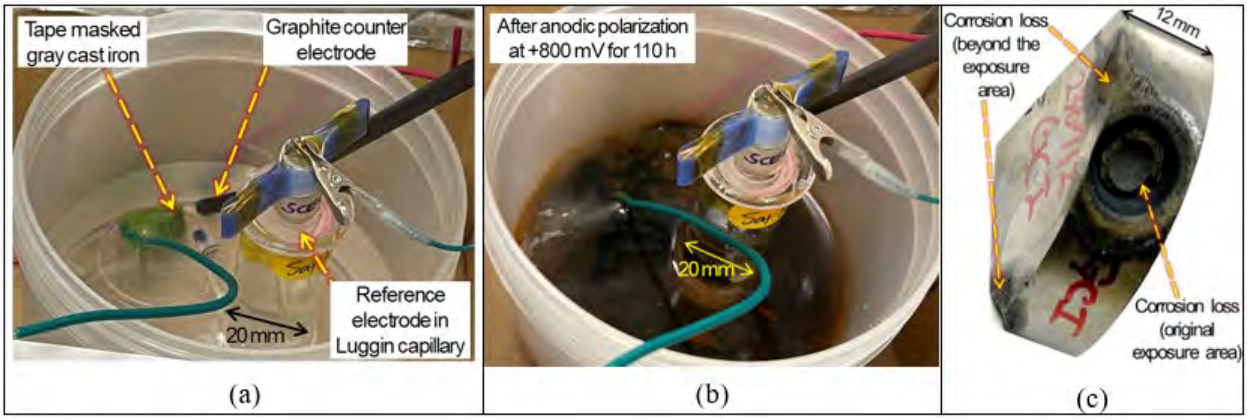

Figure 26. (a) Electrochemical setup for anodic polarization of a GCI sample, (b) a photo image showing significant dissolution of Fe in the solution (darker orange color) after anodic polarization for 110 h, and (c) the GCI sample after polarization showing apparent corrosion volume loss form the initial exposure area.

Figure 27a shows anodic current transients from two GCI samples polarized at 800 and 300 mV above the naturally-forming corrosion potentials. As expected, the anodic current was greater in the polarization at 800 mV compared to 300 mV. With increasing exposure time, the anodic current gradually decayed under 800 mV polarization, implying that the rate of Fe dissolution decreased by ohmic drop, possibly from the formation of relatively dense corrosion products. On the other hand, the change of anodic current was relatively small in the GCI sample polarized at 300 mV, which could imply that the formation of relatively porous corrosion product did not limit the dissolution of Fe in this case. The total anodic charges were estimated to be 2331 and 332 coulomb (C) after the polarizations at 800 mV for 110 hours and 300 mV for 66 hours, respectively. The anodic charge was approximately 7 times greater in the former (800 mV, 110 hour) than the latter case (300 mV, 66 hour).

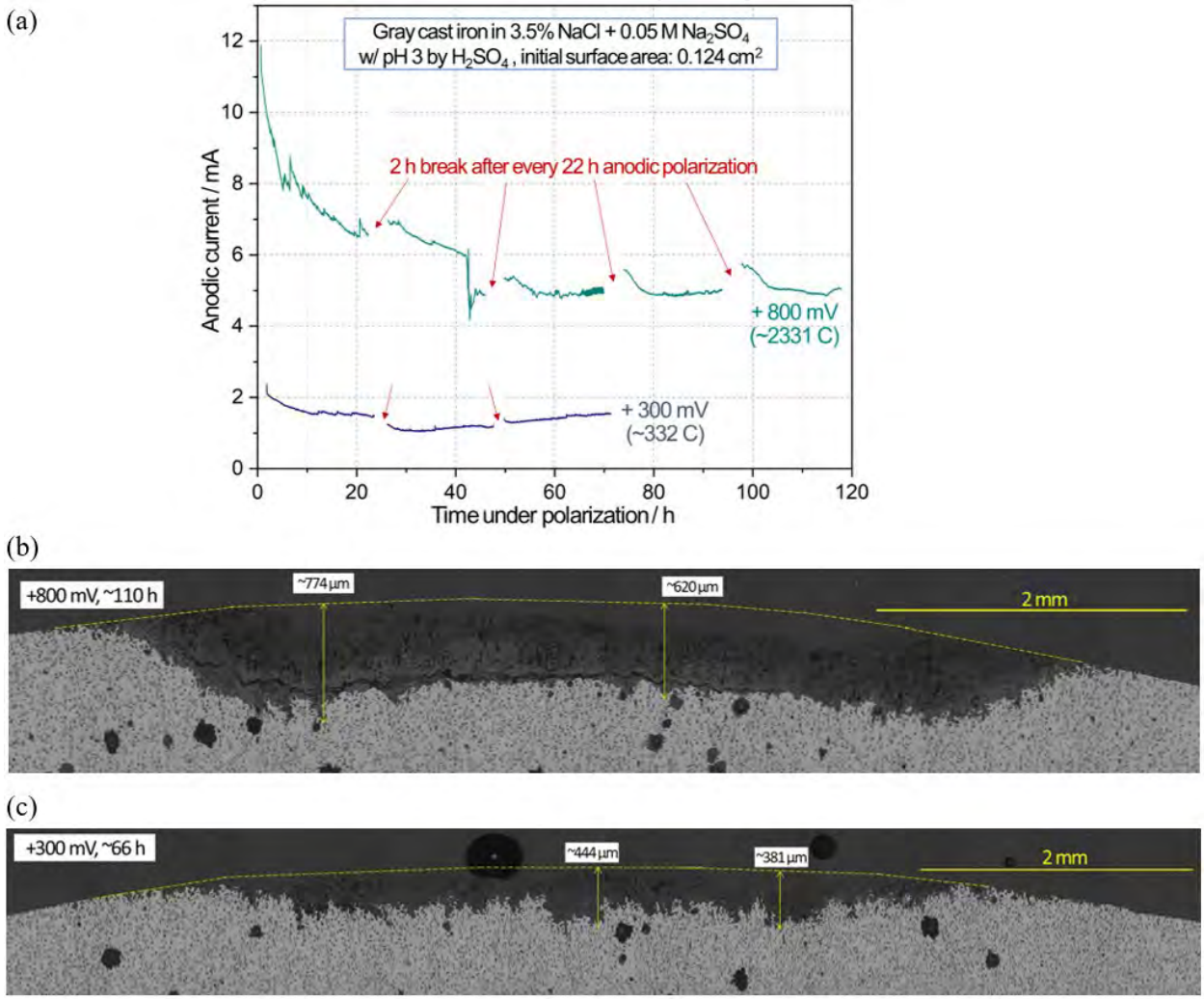

Figure 27. (a) Anodic current transients of GCI with increasing immersion time in pH 3 3.5% NaCl + 0.05 M Na_2SO_4 solution, and cross-sectioned GCI samples after (b) +800 mV for 110 h and (c) +300 mV for 66 h.

Figure 27b and Figure 27c display two optical microscope images of cross-sectioned GCI samples after 800 mV for 110 hours and 300 mV for 66 hours of polarization in the overall view perspective. The corrosion volume losses are clearly distinguished from the uncorroded locations, and the maximum corrosion depths in the images are ~774 and ~444 µm in Figure 27b and Figure 27c, respectively. Assuming linear corrosion depth growth, the corrosion rates are ~169 and ~161 µm per day for the observed maximum depths of ~774 and ~444 µm. These rates are far greater than the target rate, 5.5 µm per day, meeting the task goal of identifying accelerated corrosion methods for cast irons susceptible to selective leaching. However, it should be noted that anodic polarization of cast iron samples can be only practical for a relatively small surface area because the electric power to apply anodic polarization over a wide surface would be excessively large. Therefore, the anodic polarization method to accelerate selective leaching is recommended for a limited surface area that can be sufficiently used for other post-corrosion characterizations.

3.6 Planned Work

Our future efforts will include regular checks to see if any recent publications provide information of interest. We would also try to learn more about the actual exposure environments of pipes that see service in reactor applications. We will examine any pipe sections expected from reactor sites where pipes had to be replaced or because the reactor is being shut down. These pipes will most likely be cast iron but we also expect to see some brass or bronze pipes.

We propose to expand our laboratory corrosion studies to include both cast irons and copper-based alloys. We will expand the test environments to include application of anodic potentials over wider potential ranges as well as different test durations. Evaluation of test environments will include other chemical environments to address the differences in corrosion resistance of the cast irons versus brass alloys versus bronze alloys. Post-exposure examinations will continue to include metallographic examination as well as SEM-EDS determination of the composition of corrosion products as well as the extent of selective removal of specific elements from the alloys.

4. ONLINE MONITORING FOR SELECTIVE LEACHING OF UNDERGROUND PIPING IN NUCLEAR POWER PLANTS

Underground piping systems in NPPs are affected by several degradation mechanisms. Selective leaching has been recognized as one of the important degradation mechanisms among these [24]. Selective leaching results in the loss of one element from a solid alloy because of corrosion. NPPs have AMPs intended to specifically inspect for the presence of selective leaching in susceptible material and environment combinations. Several inspection techniques have been developed and implemented in practice to detect and localize leaching. These include [24] destructive examination, visual inspection, mechanical testing (scratch testing), ultrasonic methods, and electromagnetic methods. Since the rate of leaching depends on the material characteristics of the pipe as well as the surrounding environment, underground pipes are categorized based on the pipe material and the soil (underground environment) type. Destructive examination of a few samples obtained from pipes in each material-environment category is the most widely practiced method. Obtaining samples for conducting destructive tests is logistically challenging because it requires digging up buried pipes, stopping plant operation, etc. Nondestructive evaluations (NDEs) also face similar logistical challenges because the testing equipment needs to be in contact with the surface of the pipe being evaluated.

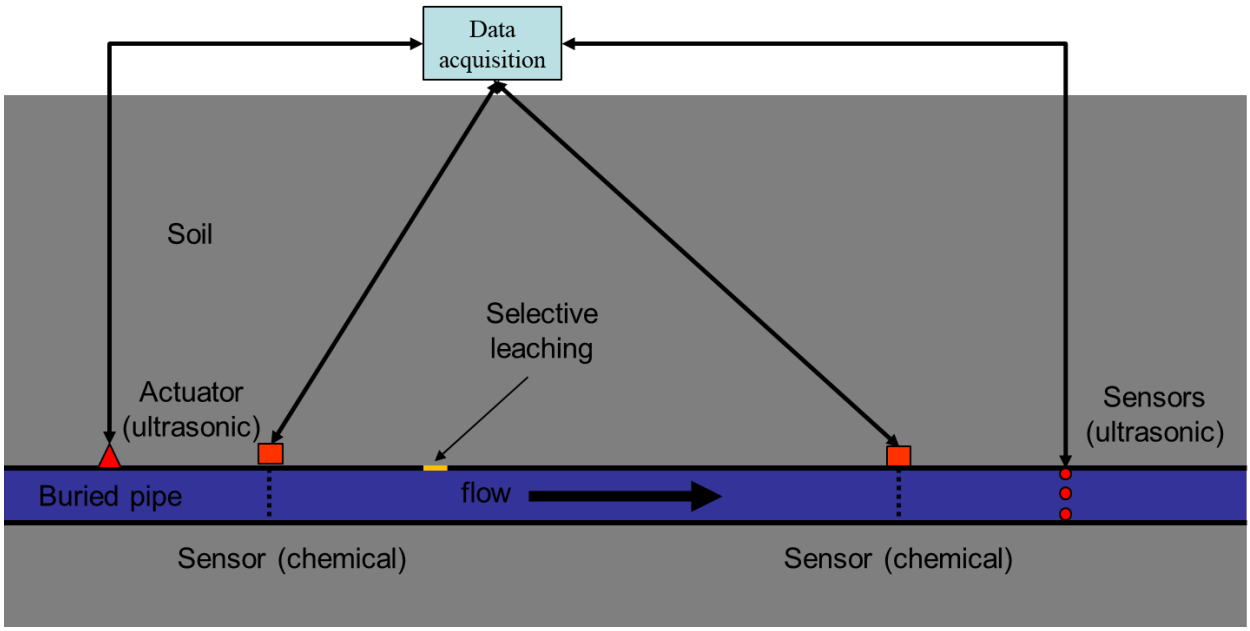

Figure 28. Online monitoring for selective leaching.

Here, we investigate the feasibility of two techniques for efficient and continuous online monitoring of underground pipes, thus overcoming the logistical bottlenecks in the current practice: (a) sensing the chemical changes in the pipe fluid (water) due to leaching and (b) sensing changes in the pipe's mechanical properties (e.g., stiffness) due to leaching (see Figure 28). The first method tries to detect byproducts of the corrosive leaching reaction (metal ions) in the pipe fluid and is suitable to detect leaching of the inner pipe surface. The second method aims to detect mechanical changes in the pipe by conducting ultrasonic guided wave pitch-catch tests, where the guided waves travel along the length of the pipe. This method could potentially detect leaching-induced mechanical changes on the inner or the outer surface of the pipe. Both these methods are considered in "online" mode, which requires (a) installing sensors on pipes susceptible to selective leaching, (b) acquiring data from these sensors continuously (passive mode) or during a certain time window with some known excitation (active mode), and (c) analyzing the sensor data to detect presence of leaching. In this report, we present the results of our preliminary numerical studies for ascertaining the feasibility of the proposed approaches. For the chemical sensing method, we simulate dispersion of metal ions in the pipe fluid and evaluate the utility of various ion sensors by modeling pipe flow by using a one-dimensional advection equation. For the ultrasonic sensing method, we build finite element models to simulate guided wave propagation in a metal pipe. We perform numerical experiments to study the effectiveness of this online monitoring method. The details of these numerical investigations are discussed in Section 4.1 and Section 4.2, respectively.

4.1 Sensing Metal ION Concentration Changes in Pipe Fluid

We consider GCI, which is a widely used material for underground water pipelines. The selective leaching of GCI is called graphitic corrosion, which describes the special behavior of this type of dealloying: the iron particles are removed from the material and graphite grains remain intact. The chemical equation that describes the mean chemical reaction of the graphitic corrosion is given as [24,25]:

$$Fe \rightarrow Fe^{2+} + 2e^{-} \tag{1}$$

Where

Fe = an iron atom

Fe^{2+} = an iron ion

e^{-} = an electron.

Equation (*1*) indicates that when graphitic corrosion happens, the corroded material will be converted to a metal (iron) ion and dissolve into the fluid flowing through the pipe. The amount of iron ion dissolved in the water can be estimated based on the amount of corroded alloy. Graphitic corrosion of the inner wall of the pipe thus leads to changes in the concentration of ions in the water flowing in the pipe. It is therefore viable to investigate the feasibility of an NDE method based on this observation. The method aims to detect the location and amount of graphitic corrosion based on the measured change in the ion concentration of the water flow in the pipe (see Figure 29).

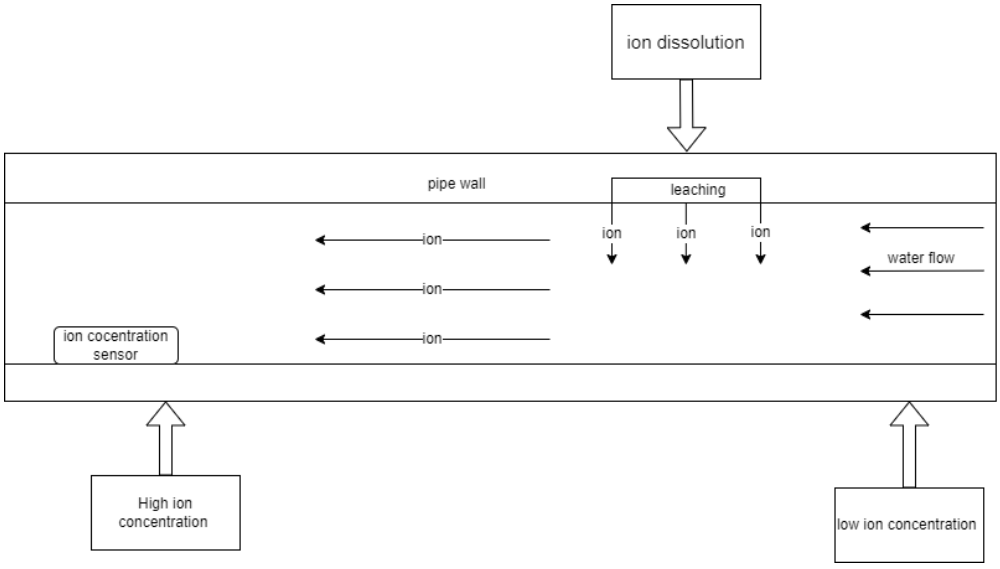

Figure 29. The schematic figure of ion concentration detection.

There are several important considerations for ascertaining the feasibility of such a method using numerical simulations. These include (a) simulating the process of ion dissolution in the pipe fluid, (b) numerical simulation of ion transport in the pipe, and (c) survey and feasibility study for available sensing modalities.

4.1.1 Ion Dissolution: Faraday's Laws of Electrolysis

Based on Faraday's laws of electrolysis [26], the corrosion rate is given by:

$$R_{corr} = \frac{i_{corr} a}{nF} \tag{2}$$

Where

R_{corr} = corrosion rate (mass loss per unit area per unit time)

i_{corr} = corrosion current density

a = atomic mass

n = valence change

F = Faraday's constant (96,485 C/mol).

For a GCI pipe, a is constant and set to be the atomic mass of the iron atom. The valence charge and corrosion current density are related to the chemical reaction. We assume the corrosion area will be the same during the process, and the material will be homogenous, so the chemical reaction will not change. Considering all the conditions mentioned in this section, it can be concluded that the corrosion rate (in terms of the number of ions dissolved into the water) is constant throughout the corrosion process. Also note that the corrosion rate in Equation (*2*), R_{corr} can be found by experiment since it is equivalent to the mass loss rate per unit area. If the rate of corrosion of the wall (the rate of thickness reduction, $\frac{dh}{dt}$) is known, then R_{corr} can be calculated as:

$$R_{corr} = \frac{dh}{dt} * \frac{A}{a} \tag{3}$$

where h is the wall thickness, t is time, A is the corroded area, and a is the atomic mass of the material.

4.1.2 Ion Transport: Advection

In previous studies [27], researchers employed the advection model to describe the transport of continuously dissolving ions in flowing water. This model is described by:

$$\frac{\partial C}{\partial t} + V_x \frac{\partial C}{\partial x} = D \left.\frac{\partial C}{\partial r}\right|_{r=dr\_} * \frac{2}{dr}, \tag{4}$$

Where

C = ion concentration ($C \coloneqq C(x,t)$)

V_x = water velocity (> 0)

x = location

dr = inside diameter of the pipe

D = diffusion constant and t is time.

It is important to note that this model assumes that the ion concentration is the same over a cross section of the pipe (i.e., the 3-D problem is simplified to a 1-D) problem. The term on the right side of Eq. (*4*)refers to the amount of ion dissolved into the water. As mentioned in Section 4.1.1 mentioned, the ion dissolution rate is constant during the whole process Hence, Eq. (*4*) can be reduced to Eq. (*5*):

$$\frac{\partial C}{\partial t} + V_x \frac{\partial C}{\partial x} = \frac{R_{corr}}{a}, \tag{5}$$

where (R_{corr}/a) is the corrosion rate (in mol/s). Equation (*5*) is the governing equation of the ion concentration change. The prediction of ion concentration change that caused by selective leaching is equivalent to the solution of Eq. (*5*). Along with the governing Eq. (*5*), we consider the following initial and mixed or Robin boundary conditions:

$$C(x,0) = 0 \; x\epsilon(0,L) \tag{6}$$

$$C(0,t) = 0 \;\; x\epsilon(0,L) \tag{7}$$

$$\frac{R_{corr}}{a} = 0 \; x\epsilon(0,l_1) \cup (l_2,L) \tag{8}$$

Equation (*6*) implies that before the leaching starts, the ion concentration of the water inside the pipe is $0\ mol/L$. Eq. (*7*) implies that the water before it does not contain any ion before entering the pipe. Equation (*8*) implies that the leaching happens only in a selected part of the pipe (from l_1 to l_2). A forward in time and centered in space (FTCS) method is used to solve Eq. (*4*). In the FTCS formulation, the finite difference method is used for numerically solving the parabolic PDE. Specifically, we employ Euler's forward time marching scheme for the time derivatives and central difference for the second-order spatial derivative.

4.1.3 Results

In the numerical simulation, the length of the pipe is set to be 10 meters (m) and the internal diameter is set to be 1 inch. We assume a scenario where the internal protective layer has been completely removed over 10% of the length (1 m), so the internal surface of this section of pipeline is the source of ions. In practice, this is an extreme case, and, in most cases, the corroded surfaces will not be so large. Under this situation, the corroded area A will be 0.07 m^2. As the pipe material is GCI, the atomic mass (a) is 26. The corrosion rate of GCI in water ($\frac{dh}{dt}$) is chosen to be 0.14mm/year according to the AGA data page [28]. Using these values, R_{corr} is calculated as 1×10^{-7} mol/s. The water velocity in the pipe is assumed to be 3 m/s, which is equivalent to 0.00152m^3/s, or 1.52L/s. The inlet water ion concentration is set to a constant of 0 mol/s. The ion dissolution due to selective leaching was set to be uniformly distributed on the inner wall of the pipe between $x = l_1$ = 1m and $x = l_2$ = 2m. The time step of the FTCS is set to be 0.005 second, and the spatial discretization step is set to be 0.1 meter. The numerical solution of ion concentration based on this model is shown in Figure 30:

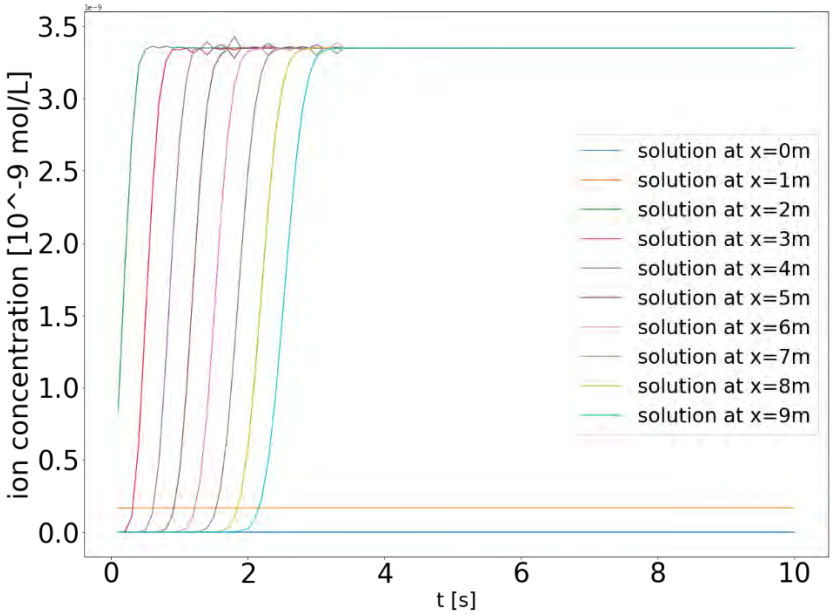

Figure 30. $\boldsymbol{Fe^{2+}}$ ion concentration in different locations in the pipe.

Figure 30 shows the ion concentration time history at 10 different locations along the pipe. Figure 30 indicates that the ion concentration at $x = 1$m and $x = 0$m will be constant; for other locations, ion concentration will also converge to 3.3×10^{-9} mol/L after sufficient time. Notice that this convergence to the steady state value occurs in 4 seconds in this numerical example.

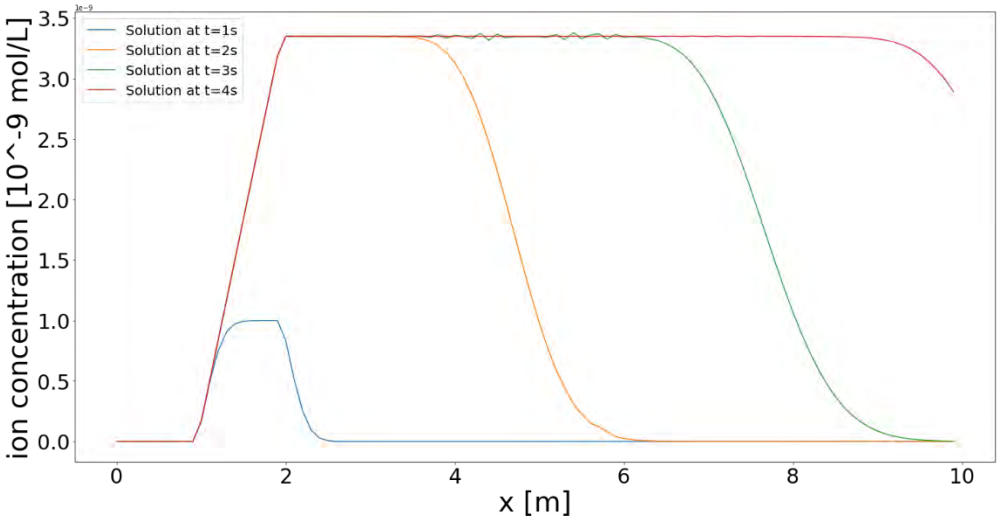

Figure 31. $\boldsymbol{Fe^{2+}}$ ion concentration in different time.

Figure 31 shows the ion concentration along the length of pipe at different times. According to Figure 31, the ion dissolution to water will form a high concentration area. In this area, the ion concentration is higher than 0 and will converges to a steady level (3.3×10^{-9} mol/L). This area of high concentration expands in the direction of the water flow at the same rate as the water flow. From the simulation results, the following observations can be made:

1. The ion concentration in the water flow does not change before the water flow passes through the leaching area. This suggests that changes in ion concentration provide direct evidence that selective leaching occurs upstream of the sensor.
2. The ion concentration increase due to selective leaching will converge to a steady state at a certain distance from the leaching site. This implies that if the leaching site is located away from the sensor, then the leaching site localization is difficult.
3. The ion concentration in the water flow will reach a steady state after some time. This suggests that if the leaching start time is longer than a certain length of time from the time the sensor detects the ion concentration, then the sensor will not be able to tell by the ion concentration level when leaching started.

4.1.4 Discussion

Although we used large (0.07 m^2) leaching area, the ion concentration is still only about 3.3×10^{-9}mol/L. Based on the review of recent literature, [29] the most sensitive on-site water ion concentration sensor has a sensitivity level of 1×10^{-5}mol/L. It is, therefore, not feasible to use an on-site ion concentration sensor to detect such small ion concentration changes. Furthermore, in the simulation, we assumed that the ion (chemical marker) concentration in the ambient pipe fluid (water) is 0 mol/L. However, tap water has the mean Fe^{2+} ion concentration of about 1×10^{-6} mol/L. The ion concentration increase caused by the selective leaching is thus too small compared to the ambient ion concentration in tap water. It may be impossible to distinguish whether the ion concentration change is caused by the leaching or due to a routine fluctuation of the ambient ion concentration. Due to these results, we conclude that this method is not a viable NDE method for online monitoring of selective leaching.

4.2 Sensing Pipe Wall Mechanical Property Changes

The ultrasonic wave propagation has been used as a pipeline inspection method for a long time [29]. Traditional ultrasonic wave inspection involves the through-thickness, pulse-echo mode to detect changes in the mechanical condition of the pipe wall. The wall thickness can be estimated using the known wave velocity and the arrival time of the reflection wave. If the measured (estimated) wall thickness shows uncharacteristically low value, then this is taken as a sign of damage in the pipe wall. This method requires access to the pipe surface at multiple locations to ascertain the integrity of the pipe. This is the main logistical difficulty in using this method for inspecting buried pipes. Here, we investigate the potential for detecting pipe mechanical property change using guided wave propagation along the length of the pipe. After selective leaching of GCI, the mechanical properties in the damaged area will closely resemble those of the residual material (graphite). A simulation study [30] has demonstrated that the presence of a small heterogeneity in a metallic component will alter the phase velocity of the guided wave. In the case of GCI damaged due to leaching, the speed of sound decreases in the graphite region formed. It is possible to determine whether graphitic corrosion has occurred in the propagation path of the sound wave based on the phase velocity of the sound wave measured by the transducer. In this report, we discuss the results of numerical simulations performed to confirm the correctness and feasibility of this method.

4.2.1 Numerical Simulation of Wave Propagation in Pipe Wall

The governing equation that describes the wave propagation is the wave equation, as

$$\nabla \cdot \boldsymbol{\sigma} = \rho \ddot{\boldsymbol{u}} \tag{9}$$

Where

u = displacement

t = time

$\boldsymbol{\sigma}$ = Cauchy stress tensor.

The solution of Equation (9), which is a second-order PDE describes the propagation of a mechanical disturbance (a wave) in a material. Here, the finite element method is used to numerically simulate guided wave propagation in a damaged and an undamaged pipe. The goal of the numerical studies is to identify the feasibility of laboratory experiments for guided wave-based detection of leaching in underground pipes. A 1-meter-long GCI pipe with an inside diameter of 3 inches and an outside diameter of 3.5 inches is considered in the numerical simulation. An excitation is applied at a point located 10 cm away from one end of the pipe and four measurement locations (finite element nodes) are situated 10 cm away from the other end. Damage is simulated in the pipe by changing material properties of a small outer section (30 mm × 30 mm × 2mm) of the pipe. Both damaged and undamaged pipe models are excited using the same dynamic force applied at the same location, and the response is measured at the same four locations. The finite element model of the pipe and the shape of the graphite region are shown in Figure 32. Table 3 shows the mechanical properties of the materials.

Table 3. Mechanical properties of pipe and selective leaching byproducts.

Material	Density (Kg/m^3)	Young's modulus (GPa)	Poisson's ratio
GCI	7150	124	0.3
Graphite	2260	11.5	0.13

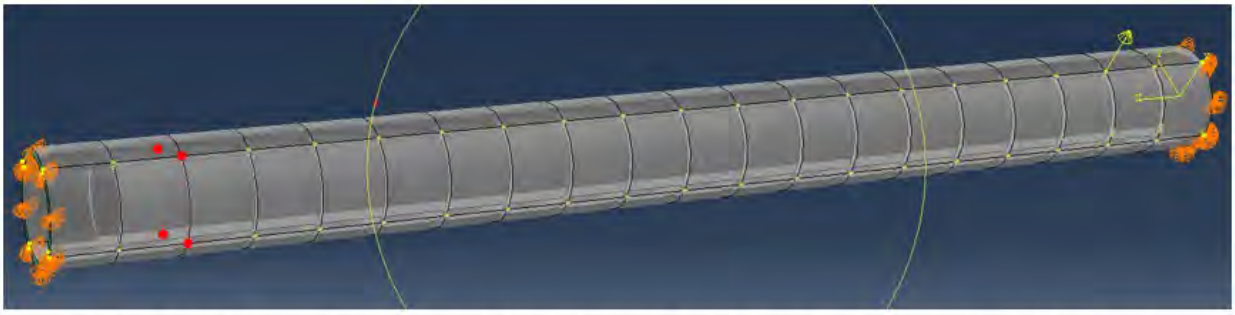

(a) Pipe model, sensor locations (red dots), dynamic point force (yellow arrow), and boundary conditions (both ends of the pipe)

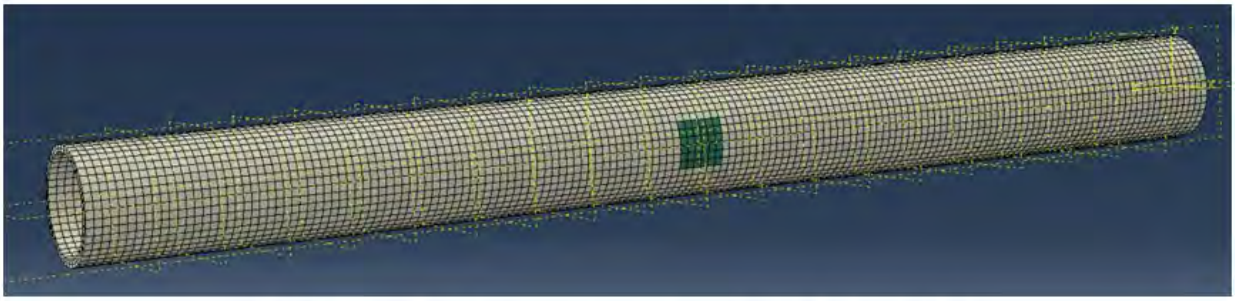

(b) Damage (leaching) zone (green), undamaged pipe (white)

Figure 32. Finite Element model and defect region.

The excitation signal is a Hanning modulated pulse signal. The mean frequency of the signal is set to 128 kHz. The wave shape of the excitation signal is shown in Figure 33:

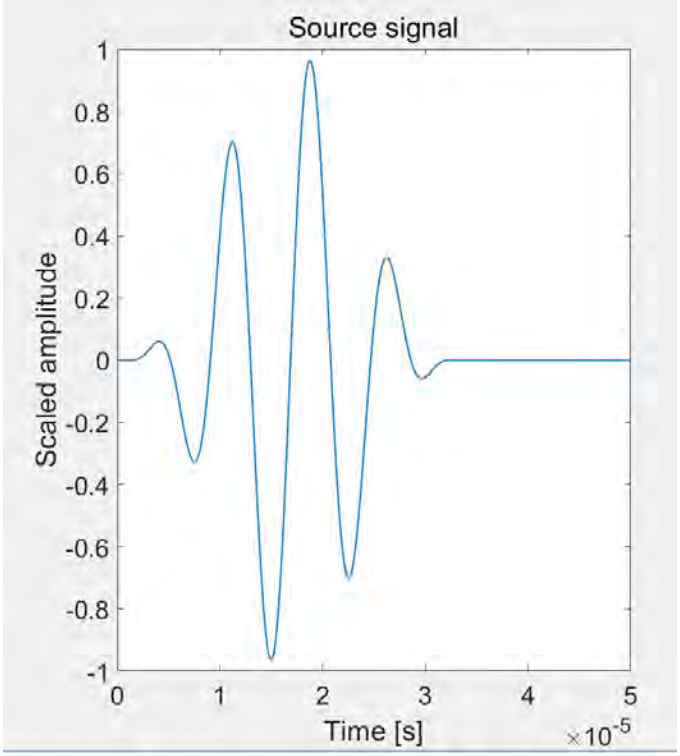

Figure 33. Excitation signal.

The finite element mesh for the pipe is shown in Figure 34: a 20-noded hexahedral element with reduced integration (C3D20R) is used for spatial discretization. The pipe model contains 20800 finite elements. Notice that the damage is simulated by changing the material properties of a few elements (see Figure 32(b)). The numerical simulation is performed using an implicit time marching scheme for a total duration of 0.5 milliseconds. The simulation results are discussed in the next section.

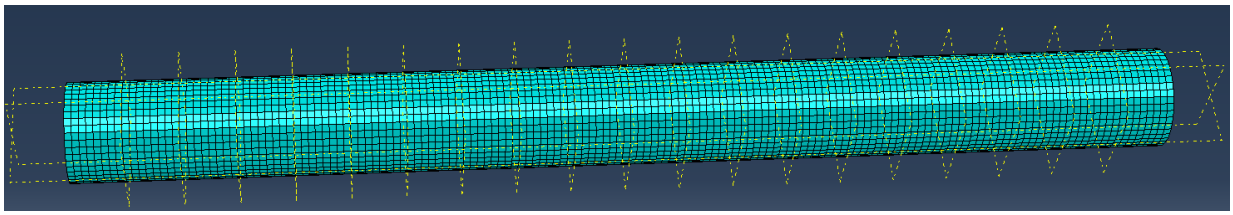

Figure 34. Finite element mesh for the pipe.

4.2.2 Results

The responses (displacements) recorded at the four measurement locations are shown in Figure 35.

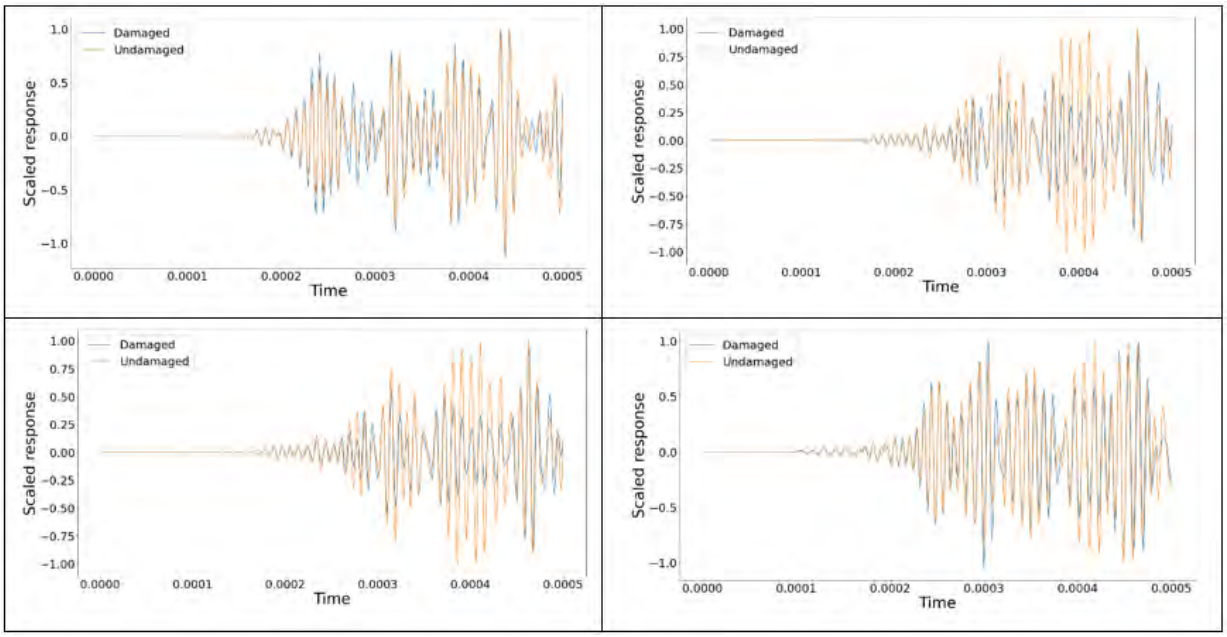

Figure 35. Recorded responses for damaged and undamaged pipe.

The main observations are:

1. The guided wave reaches the sensor at almost the same time for damaged as well as undamaged pipe. The pipe is 1 meter long, so the wave will arrive the sensor in about 2×10^{-5} s. Considering the accuracy of the data processing systems, it is not feasible to obtain accurate phase velocity data in this case (with such a small propagation time). Note that in real-world applications, where pipe length may be up to tens of meters, diagnosis based on time of arrival may be feasible.

2. It is desirable to detect selective leaching in the pipe wall *before* it penetrates through the thickness of the pipe wall. In the case of a partially leached pipe cross-section, there will be (at least) two layers of material in the pipe: the outer layer consists of the porous graphite structure left behind by corrosion and the inner layer consists of the original material of the pipe. Waves can still propagate through the inner layer, thus avoiding low velocity regions. Diagnosis of the location and size of the low velocity region could be challenging because of this effect.
3. There is a significant difference in the amplitude of the two signals. The difference in amplitude indicates the difference in mechanical energy reaching the measurement location. The mechanical energy contained in the wave is dissipated by refraction and reflection as the wave passes through the damage zone. This indicates that the difference in amplitude of the received wave can be used to detect leaching damage. Specifically, in graphitic corrosion detection, this method can be used to determine whether the pipe cross-section in the wave path is composed entirely of ductile iron or contains regions composed of porous graphite.

4.3 FUTURE WORK

The future work consists of:

1. Experimentally investigate the method discussed in Section 4.2. We have acquired three ductile iron pipe samples (donated by the ORNL – see Figure 36). We will remove the outer tar layer on these pipes, induce leaching over a small region using a localized chemical treatment, instrument the pipes with actuators and sensors, bury them in a sand box, and conduct experiments to investigate the effectiveness of the proposed methodology.

Figure 36. Ductile iron pipe samples.

2. Include actuation and sensing physics in the finite element analysis models to make more realistic numerical simulations of the proposed test procedure. This will help conduct the optimal sensor and actuation placement investigations. We will also consider more realistic damage severities and multiple model geometries as well as locations.
3. Build machine-learning models to learn the pattern in damaged and undamaged pipes using the data obtained from numerical simulation. This physics-informed machine-learning approach could help in developing an advanced diagnostic tool for real-world applications.
4. Explore optimal actuation configuration. For underground pipes, we can use a ring actuator(s) around the pipe to simulate the excitation on the cross section. In future, we will simulate the ring actuator response and the cross-section excitation response and decide whether we will update to a ring actuator or not.

5. SUMMARY

The unique structure of MOOSE and the applications built on this framework lend themselves to a rapid, efficient development of model simulations, and a future path in determining relative probability of failure. Significant development in modeling selective leaching for GCI has been done, with further refinements planned. The preliminary results show a high-fidelity representation of the physics involved in the process. Determining accurate failure probability distributions should be a straightforward path using MOOSE tools and methods discussed in Section 2.

Review of the documents provided by EPRI as well as open literature reports provided information on studies that have been conducted, as well as techniques which could be employed to assess the extent of corrosion. Some of the open literature documents provided to us addressed fracture toughness and mechanical testing of cast iron pipe materials.

Although we were only able to obtain the one check valve with actual reactor exposure, we were able to examine sections of the check valve as well as water pipes which had been in service for decades at ORNL. These examinations showed formation of one or more iron oxides, and in the case of the water pipes, complete penetration of an approximately 1 cm (~3/8") wall. Preferential attack leading to wall penetration was found on the surface of pipes that were inadvertently exposed to water containing dissolved deicing salt.

Laboratory corrosion studies found that NaCl solutions as well as solutions containing both NaCl and Na_2SO_4 caused significant corrosion of GCIs and DCIs in hundreds of hours. Very limited studies showed that application of an anodic potential may have greatly accelerated corrosion of GCI in an aqueous solution of 3.5% NaCl + 0.05 M Na_2SO_4.

In this report, we discussed initial investigations into the feasibility of two methods for online monitoring of leaching in underground pipes. We developed a mathematical model for metal ion diffusion and advection to investigate detection feasibility for graphite corrosion of the inner pipe wall. We quantified the changes in the ion concentration of the pipe fluid (water) in the case of corrosion of the pipe wall. The simulation results show that it is not feasible to detect or localize leaching by sensing the metal ion concentration in the pipe water. Currently available metal ion sensors are simply not sensitive enough to allow such detection and localization. We also built a finite element model of the pipe and simulated the propagation of acoustic waves (pitch-catch along the length of the pipe) in the pipe. Using these numerical simulations, some characteristics of sound wave propagation in corroded pipes were found and the feasibility of detecting pipe corrosion through these characteristics was verified.

6. REFERENCES

1. Gaston, D., et al. 2009. "MOOSE: A parallel computational framework for coupled systems of nonlinear equations." *Nuclear Engineering and Design*, **239**, 1768-1778. https://doi.org/10.1016/j.nucengdes.2009.05.021.

2. Lindsay, A., et al. 2022. "2.0 - MOOSE: Enabling massively parallel multiphysics simulation." *SoftwareX*, **20**. 101202. https://doi.org/10.1016/j.softx.2022.101202.

3. Jiang, W., Spencer B. and Dolbow, J. 2019. "Ceramic Nuclear Fuel Fracture Modeling with the Extended Finite Element Method." *Engineering Fracture Mechanics*, **223**. 106713. https://doi.org/10.1016/j.engfracmech.2019.106713.

4. Ahrens, J., Geveci, B., and Law, C. 2005. "36-ParaView: An End-User Tool for Large Data Visualization." in *Visualization Handbook*. Elsevier, ISBN 978-0123875822. https://doi.org/10.1016/B978-012387582-2/50038-1.

5. Kittl, P., Diaz, G., and Morales, M. 1990. “Determination of Weibull’s parameters on flexure strength of round beams of aluminum-copper alloy and cast iron.” *Theoretical and Applied Fracture Mechanics*, **13**, no. 3, pp. 251-255. ISSN 0167-8442. https://doi.org/10.1016/0167-8442(90)90092-E.

6. Yan, G., et al. 2023. “Transport mechanisms of hydrothermal convection in faulted tight sandstones.” *Solid Earth*, **14**, no 3. https://se.copernicus.org/articles/14/293/2023/

7. Debnanth, S., et al. 2021. “Material properties for fracture mechanics based strength assessment of cast iron water mains.” *Canadian Journal of Civil Engineering*, **48**, no 1. https://doi.org/10.1139/cjce-2019-0229.

8. Jiang, R., et al. 2019. “Analysis of failure initiation in corroded cast iron pipes under cyclic loading due to formation of through-wall cracks.” *Engineering failure analysis*, **103**, 238-248. https://doi.org/10.1016/j.engfailanal.2019.04.031.

9. J Ji, C Zhang, J Kodikara, S-Q Yang. 2015. “Prediction of stress concentration factor of corrosion pits on buried pipes by least squares support vector machine.” *Engineering Failure Analysis*, **55**, https://www.sciencedirect.com/science/article/pii/S1350630715001600.

10. Mohebbi, H., et al. 2010. “The fracture and fatigue properties of cast irons used for trunk mains in the water industry.” *Mater. Sci. Eng. A*, **527**, no. 21-22, 5915-5923. https://doi.org/10.1016/j.msea.2010.05.071.

11. Fahimi, A., et al. 2016. “On the residual strength of aging cast iron trunk mains: Physically based models for asset failure.” *Mater. Sci. Eng. A*, **663**, 204-212. https://doi.org/10.1016/j.msea.2016.03.029.

12. Ugoh, G., et al. 2019. “On the residual strength of ageing cast iron wastewater assets: Models for failure.” *Mater. Sci. Eng. A*, **768**, 138221. https://doi.org/10.1016/j.msea.2019.138221.

13. Mohebbi, H., et al. 2009. “Characterization of the fatigue properties of cast irons used in the water industry and the effect on pipe strength and performance.” *J. Physics: Conference Series*, **181**, no. 1, 012039. http://dx.doi.org/10.1088/1742-6596/181/1/012039.

14. Antaki, G. 2018. “Roadmap to Integrity Evaluation and Repair of Nuclear Plant Piping.” Electric Power Research Institute, Palo Alto, CA: EPRI Report 3002013156, pp134. https://www.epri.com/research/products/000000003002013156.

15. Wong, E., et al. 2022. “Leveraging Risk Insights for Aging Management Program Implementation: 2022.” Electric Power Research Institute, Palo Alto, CA. EPRI Report 3002020713, pp. 126. https://www.epri.com/research/products/000000003002020713.

16. Jenks, A. 2021. “Accelerated Testing and Evaluation of Factors Affecting Selective Leaching Susceptibility.” Electric Power Research Institute, Palo Alto, CA: 2021 EPRI Report 3002020822. https://www.epri.com/research/programs/065756/results/3002020822.

17. Sears, E. C. 1968. “Comparison of the Soil Corrosion Resistance of Ductile Iron Pipe and Gray Cast Iron Pipe.” *Materials Performance*, 33.

18. Rajani, B., Zhan, C., and Kuraoka, S. 1996. “Pipe-Soil Interaction Analysis of Jointed Water Mains.” *Canadian Geotechnical Journal*, **33**, no. 3, 292. https://doi.org/10.1139/t96-061.

19. Makar, J. M. 2000. “A preliminary analysis of failures in grey cast iron water pipes.” *Engineering Failure Analysis*, **7**, 43-53. https://doi.org/10.1016/S1350-6307(99)00005-9.

20. Jesson, D. A., et al. 2013. “On the condition assessment of cast iron trunk mains: the effect of microstructure and in-service graphitization on mechanical properties in flexure.” *Mater. Sci. Eng. A*, **576**, 192-201. https://doi.org/10.1016/j.msea.2013.03.061.

21. Cilluffo, G. 2014. “Piping Corrosion Rate & Remaining Life Basis: Commercializing Conservatism in First time Inspections.” *Proceedings of the ASME 2014 Pressure Vessels & Piping Conference*. *Volume 1: Codes and Standards*. Anaheim, CA: (July 20–24). PVP2014-28781. https://doi.org/10.1115/PVP2014-28781.

22. Jun, J., et al. 2019. “Methodologies for Evaluation of Corrosion Protection for Ductile Iron Pipes.” Oak Ridge National Laboratory. ORNL/TM-2017/144. https://info.ornl.gov/sites/publications/Files/Pub73746.pdf.

23. Keiser, J. et al. n.d. “Examination of Failed Process Water Pipes.” Internal Report, Oak Ridge National Laboratory.

24. EPRI. 2019. “Selective Leaching State-of-the-Art.” Electric Power Research Institute Technical Update, 3002016057. https://www.epri.com/research/programs/065756/results/3002016057.

25. McCue, I., et al. 2016. “Dealloying and Dealloyed Materials.” *Annual Review of Materials Research*, **46**, 263-286. https://doi.org/10.1146/annurev-matsci-070115-031739 .

26. Ahmad, Z. 2005. “Principles of Corrosion Engineering and Corrosion Control.” Butterworth-Heinemann. 57-119.

27. Zielina, M., Bielski, A., and Młyńska, A. 2022. “Leaching of chromium and lead from the cement mortar lining into the flowing drinking water shortly after pipeline rehabilitation.” *Journal of Cleaner Production*. 362, 132512. https://doi.org/10.1016/j.jclepro.2022.132512.

28. Frank, P. 1994. “Corrosion Resistance of Zinc and Zinc Alloys.” Routledge and CRC Press. 524. ISBN 9780824792138. https://www.routledge.com/Corrosion-Resistance-of-Zinc-and-Zinc-Alloys/Porter/p/book/9780824792138.

29. Chen C., et al. 2019. “Self-powered on-line ion concentration monitor in water transportation driven by triboelectric nanogenerator.” *Nano Energy*, **62**, 442-448. https://doi.org/10.1016/j.nanoen.2019.05.029.

30. Zou, F., & Cegla, F. B. 2018. “On quantitative corrosion rate monitoring with ultrasound.” *Journal of Electroanalytical Chemistry*, **812**, 115-121. https://doi.org/10.1016/j.jelechem.2018.02.005.